AGU PUBLICATIONS

Geochemistry, Geophysics, Geosystems

RESEARCH ARTICLE

10.1002/2014GC005450

Key Point:

- Influences of surface processes on the fold pattern in fold-and-thrust belts

Correspondence to:
M. Collignon,
marine.collignon@erdw.ethz.ch

Citation:
Collignon, M., B. J. P. Kaus, D. A. May, and N. Fernandez (2014), Influences of surface processes on fold growth during 3-D detachment folding, *Geochem. Geophys. Geosyst.*, *15*, doi:10.1002/2014GC005450.

Received 9 JUN 2014
Accepted 29 JUL 2014
Accepted article online 31 JUL 2014

Influences of surface processes on fold growth during 3-D detachment folding

M. Collignon[1], B. J. P. Kaus[2], D. A. May[3], and N. Fernandez[2]

[1]Geological Institute, ETH Zurich, Zurich, Switzerland, [2]Institut für Geowissenschaften, Johannes Gutenberg-Universität, Mainz, Germany, [3]Institute of Geophysics, ETH Zurich, Zurich, Switzerland

Abstract In order to understand the interactions between surface processes and multilayer folding systems, we here present fully coupled three-dimensional numerical simulations. The mechanical model represents a sedimentary cover with internal weak layers, detached over a much weaker basal layer representing salt or evaporites. Applying compression in one direction results in a series of three-dimensional buckle folds, of which the topographic expression consists of anticlines and synclines. This topography is modified through time by mass redistribution, which is achieved by a combination of fluvial and hillslope erosion, as well as deposition, and which can in return influence the subsequent deformation. Model results show that surface processes do not have a significant influence on folding patterns and aspect ratio of the folds. Nevertheless, erosion reduces the amount of shortening required to initiate folding and increases the exhumation rates. Increased sedimentation in the synclines contributes to this effect by amplifying the fold growth rate by gravity. The main contribution of surface processes is rather due to their ability to strongly modify the initial topography and hence the initial random noise, prior to deformation. If larger initial random noise is present, folds amplify faster, which is consistent with previous detachment folding theory. Variations in thickness of the sedimentary cover (in one or two directions) also have a significant influence on the folding pattern, resulting in linear, large aspect ratio folds. Our simulation results can be applied to folding-dominated fold-and-thrust belt systems, detached over weak basal layers, such as the Zagros Folded Belt.

1. Introduction

Over the past decades, the interactions between surface processes and development of mountain belts have been extensively studied. While syntectonic sedimentation appears to control the external development of fold-and-thrust belts [*Bonnet et al.*, 2007; *Fillon et al.*, 2013; *Simpson*, 2006], erosion strongly influences the evolution of internal regions within mountain belts by enhancing crustal uplift and exhumation of rocks in convergent orogens [e.g., *Beaumont et al.*, 1992; *Burbank*, 2002; *Kaus et al.*, 2008; *Molnar and England*, 1990; *Montgomery and Brandon*, 2002]. The effects of sedimentation and/or erosion on brittle deformation have been studied using analogue [e.g., *Graveleau*, 2008; *Konstantinovskaia and Malavieille*, 2005; *Malavieille*, 2010; *Mugnier et al.*, 1997; *Persson and Sokoutis*, 2002; *Storti and McClay*, 1995] and numerical [e.g., *Avouac and Burov*, 1996; *Beaumont et al.*, 1992; *Kooi and Beaumont*, 1994; *Willett*, 1999, 2010] models of accretionary wedges. With some notable exceptions [*Braun and Yamato*, 2010; *Thieulot and Huismans*, 2011], most numerical studies employed a 2-D mechanical model, restricting the surface processes model to 1-D [*Avouac and Burov*, 1996; *Fillon et al.*, 2013; *Willett*, 1999, 2010]. Also, the surface processes models often used a simple linear diffusion formulation [*Avouac and Burov*, 1996; *Kooi and Beaumont*, 1994] or a formulation where both sedimentation and erosion are rarely present together [*Fillon et al.*, 2013; *Willett*, 1999, 2010].

In order to fully understand how surface processes influence the internal deformation pattern of the orogen, or the fold-and-thrust belt, as well as predicting the sediment routing system, 3-D mechanical models are required. Due to the computational challenges associated with performing fully 3-D mechanical simulations, thin-sheet models have been frequently used [*Simpson*, 2004a, 2004b, 2004c]. As thin-sheet models depth average the rheology and density of all layers, the true coupling between surface processes and multilayer systems cannot be completely understood. To date, very few studies have coupled sophisticated surface processes models, which can treat both deposition and erosion, with fully 3-D mechanical models [*Braun and Yamato*, 2010; *Ruh et al.*, 2013; *Thieulot and Huismans*, 2011]. These models focused on the effects of a

10.1002/2014GC005450

Table 1. Physical Parameters Used by the Coupled Model

Symbol	Unit	Definition
Lx, Ly, Lz	m	Initial dimensions of the model in x, y, and z
x, y, z	m	Coordinates
z_ref	m	Reference level
H	m	Maximum initial elevation
h_0	m	Initial roughness of the surface processes model
C	$(m^2\ s^{-1})^{1-n}$	Fluvial incision
K	$m^2\ s^{-1}$	Hillslope diffusion
N		Exponent for dependency of sediment transporton Fluid discharge
A	$m\ s^{-1}$	Annual rainfall
Q	$m^2\ s^{-1}$	Surface fluid discharge
B		Regional slope (defined by H/Ly)
H	Pa s	Viscosity
G	$M\ s^{-2}$	Gravity
Δ	$kg\ m^{-3}$	Density
ε_{yy}	s^{-1}	Background strain rate (in *y* direction)

brittle overburden rheology, which is mostly applicable to thrust-dominated fold-and-thrust belts or brittle orogens.

In contrast, the influence of surface processes on ductile deformation has been much less investigated. Thin-skinned fold-and-thrust belts are seen as the compressional deformation of a sediment pile over a weak layer acting as a décollement. The resulting surface expressions have often been interpreted, based on geometrical criteria in terms of fault bend folds, fault propagation folds, or/and detachment folds.

Recently, it was demonstrated [*Yamato et al.*, 2011] that mechanically there is a difference between fold-dominated and fault-dominated fold-and-thrust belts. A fold-dominated fold-and-thrust belt develops if a folding instability can grow in a relatively short amount of time. The fold growth rates can be accelerated by the presence of weak layers in an otherwise brittle overburden [*Ruh et al.*, 2012; *Yamato et al.*, 2011]. If on the other hand, folds grow too slow, faulting/thrusting dominates the deformation. Several analogue studies have demonstrated that sedimentation can influence the shape and the growth of folds as well as the development of faults on one or two sides of a growing fold [*Barrier et al.*, 2002; *Nalpas et al.*, 1999; *Nalpas et al.*, 2003; *Pichot and Nalpas*, 2009]. However, coupled analogue models of ductile deformation and erosion are challenging due to material (e.g., silicone is difficult to "erode") and scaling (e.g., the characteristic time scale of surface processes is significantly different from the characteristic time scale of tectonic processes) issues. Furthermore, they often only represent the two end-member cases (e.g., no erosion versus infinitely fast erosion). They thus fail to explore the transitional cases.

Here we focus on fold-dominated fold-and-thrust belts, such as the Zagros Simply Folded Belt and study how surface processes influence the development of 3-D detachment folding patterns. We employ a fully 3-D mechanical model coupled to an erosion and sedimentation model.

2. Numerical Model

In order to study the feedback between surface processes and ductile deformation, we have developed a finite element-based landscape evolution model, which includes both sedimentation and erosion. The landscape evolution model was coupled to the 3-D parallel (distributed memory) mechanical code Lithospheric and Mantle Evolution Model (LaMEM) [*Kaus et al.*, 2012; *Popov and Kaus*, 2013]. Our mechanical models are coupled to the surface processes model, which implies that both models can influence each other. Both codes were written using the PETSc library [*Balay et al.*, 2012], and can run on massive parallel machines with a large choice of iterative solvers and preconditioners. In the following sections, we describe the individual mechanical and surface processes model (SPM) and the manner in which they are coupled. Physical parameters used in the simulations are described in Table 1.

2.1. Mechanical Model (LaMEM)

LaMEM solves the equations describing the conservation of momentum and mass for a highly viscous, incompressible fluid. Using the relationship between the total (σ_{ij}) and deviatoric (σ'_{ij}) stress tensor, the conservation of momentum for highly viscous flow (i.e., Stokes equation of slow flow) can be written as:

$$\frac{\partial \sigma'_{ij}}{\partial x_j} - \frac{\partial P}{\partial x_i} + \rho g_i = 0, \tag{1}$$

where *i* and *j* refer to the three spatial coordinates *x*, *y*, and *z*, respectively; g_i is the *i*th component of the gravity vector $\vec{g} = (g_x, g_y, g_z)$. $P = -\frac{1}{3}\ (\sigma_{xx} + \sigma_{yy} + \sigma_{zz})$ is the total pressure and ρ is the density. Stresses and the pressure are related via: $\sigma_{ij} = \sigma'_{ij} - P\delta_{ij}$, where δ_{ij} is the Kronecker delta.

10.1002/2014GC005450

The conservation of mass, assuming incompressibility is given by:

$$\frac{\partial v_i}{\partial x_i}=0. \tag{2}$$

In this work, we consider linear viscous materials with the following constitutive relationship:

$$\sigma'_{ij}=2\eta\dot{\varepsilon}_{ij}, \tag{3}$$

where

$$\dot{\varepsilon}_{ij}=\frac{1}{2}\left(\frac{\partial v_i}{\partial x_j}+\frac{\partial v_j}{\partial x_i}\right), \tag{4}$$

is the strain rate tensor and η is the shear viscosity. Equations (1–4) are discretized using a finite difference staggered grid method. In most models, here, we employed a parallel direct solver MUMPS [*Amestoy et al.*, 2000; *Lechmann et al.*, 2011] in combination with Powell-Hesteness iterations to enforce the incompressibility constraint. For the high-resolution simulations, we used the GCR Krylov method [*Eisenstat et al.*, 1983] with an algebraic multigrid preconditioner BoomerAMG which is part of the HYPRE package [*Falgout et al.*, 2013]. We approximate a free surface with a combination of an internal surface and a zero-density, low-viscosity sticky-air layer, which was recently demonstrated to be a good approximation of a true free surface [*Crameri et al.*, 2012]. We found this to be of advantage in combination with an Eulerian finite difference approach as there are no complications due to a strongly deformed erosional valley, which can result in sharply deformed surface topography that would require remeshing if a Lagrangian finite element method was employed.

2.2. Surface Process Model (SPM)

On a large scale (e.g., mountain belt), topography evolution, h, can be expressed as a time-dependent surface subject to the conservation of sediment and water, and a transport law, $q_{sed} = F(S, q)$, where the surface sediment discharge ($m^2\ s^{-1}$), q_{sed} is a function of the local slope $S = |\nabla h|$, and water discharge q [*Smith and Bretherton*, 1972]. The sediment transport law we use, assumes that the system is transport limited, i.e., the sediment supply exceeds the sediment transport capacity [*Whipple and Tucker*, 2002], implying that deposition will occur along the river. This approach differs from the classical stream-power law [*Braun and Willett*, 2013; *Howard and Kerby*, 1983; *Whipple and Tucker*, 1999], which considers detachment-limited conditions, where the sediment transport capacity exceeds the sediment supply, and thus, the channel bedrock is always eroded.

The stream-power law formulation in itself only reflects fluvial incision, implying that every point in the landscape is within a channel. As a result, models that use this formulation [*Braun and Willett*, 2013; *Willett*, 2010] do not account for parts of the landscape such as hillslopes, channel heads, and upper channels, where nonfluvial processes (e.g., debris flow) dominate over incision. Hillslopes could be however introduced either in an analytical manner [*Goren et al.*, 2014], or they could be taken into account by simply adding a linear diffusion term to the stream-power equation. Furthermore, the stream-power law does not account for the deposition of sediments either. A threshold on the fluid discharge could be applied in order to allow sedimentation along the river [*Davy and Lague*, 2009], or to counter the routing problem that arises from local minima (e.g., lakes) when the water algorithm only considers one receiver [*Garcia-Castellanos et al.*, 2003; *Goren et al.*, 2014]. Using a diffusion formulation naturally accounts for both erosion and sedimentation simultaneously, and can slightly reduce the routing problem due to local minima, although it does not counter it. Moreover, the expression of the sediment discharge includes a term for both hillslope processes and fluvial incision. However, it should be kept in mind that this model uses a simple formulation and thus neglects certain aspects such as landslides or detachment-limited conditions, which can have a great influence on the morphologic evolution of landscapes [*Tucker and Whipple*, 2002]. As we here focus on the effects of mass transfer on the folding pattern in a fold-and-thrust belt setting, the sediment transport law proposed in this paper seems to be at this scale a good approximation. If one wants to capture geomorphic features such as rivers capture, or knickpoint migration, the use of a stream-power law formulation would be more appropriate.

We follow the formulation of *Simpson and Schlunegger* [2003], in which the surface processes model is governed by a system of two equations with two unknown functions, the topography $h(x, y, t)$, and the surface water discharge $q(x, y, t)$. The system of equations describing the evolution of topography is given by:

 10.1002/2014GC005450

$$\frac{\partial h}{\partial t} = -\nabla \cdot (\mathbf{n} q_{sed}), \tag{5}$$

$$\nabla \cdot (\mathbf{n} q) = \alpha \ , \tag{6}$$

where $\mathbf{n} = -\nabla h / S$ is a unit vector directed down the surface, α is the effective rainfall (in excess of infiltration), and q_{sed} is the surface sediment discharge.

In our models, we use a simple formulation [*Simpson and Schlunegger*, 2003] for the sediment discharge that enable to model both dispersive (i.e., hillslope diffusion) and concentrated (i.e., fluvial incision) effects of erosion due to water runoff. This formulation can be applied on the entire surface without distinguishing between channels or hillslopes. The sediment discharge is defined as:

$$q_{sed} = cq^m S + kS, \tag{7}$$

where k is the hillslope diffusivity ($m^2 s^{-1}$), c is the fluvial incision coefficient ($(m^2 s^{-1})^{1-m}$), and m is an exponent quantifying the relationship between sediment and water discharge. The first term represents the fluvial transport of sediments, while the second term relates to the dependency of flux to local slope [*Culling*, 1960].

Substituting equation (7) into equation (5), gives:

$$\frac{\partial h}{\partial t} = \nabla \cdot ((cq^m + k)\nabla h), \tag{8}$$

$$\nabla \cdot \left(\frac{\nabla h}{|\nabla h|} q \right) = -\alpha. \tag{9}$$

Note that the sediment discharge q_{sed} has the dimension of the diffusion coefficient.

Equation (8) is discretized in space using the Galerkin finite element method [*Zienkiewicz and Taylor*, 2000]. The domain is partitioned into a set of nonoverlapping quadrilateral elements. The mesh contains elements of constant size Δx and Δy. Over each element, we employ bilinear shape functions (denoted $N(x, y) = [N_1(x, y)\ N_2(x, y)\ N_3(x, y)\ N_4(x, y)]$) to approximate the height, h, in term of nodal variable H_i:

$$h(x, y) \approx [N_1(x, y)\ N_2(x, y)\ N_3(x, y)\ N_4(x, y)]\ [H_1\ H_2\ H_3\ H_4]^T = NH_e,$$

where T indicates the transpose operator.

The weak form of diffusion problem is obtained by multiplying equation (8) by the shape functions, substituting $h = NH_e$ and integrating over the element volume Ω_e, yielding to:

$$\int_{\Omega_e} N^T \frac{\partial}{\partial t} (NH_e)\ dV = \int_{\Omega_e} N^T \nabla^T (D\nabla N) H_e\ dV, \tag{10}$$

with $D = cq^m + k$, the diffusion coefficient.

Using integration by parts over the domain Ω_e and considering Neumann boundary conditions, equation (10) can be simplified by:

$$M_e \left(\frac{\partial H_e}{\partial t} \right) + K_e H_e = F_e, \tag{11}$$

$$\text{where } M_e = \int_{\Omega_e} N^T N\ dV, \tag{12}$$

$$K_e = -\int_{\Omega_e} (\nabla N)^T D \nabla N\ dV, \tag{13}$$

$$F_e = \oint_{\Gamma_e} N^T \hat{q}^T n\ dS, \tag{14}$$

where M_e and K_e are the element stiffness matrices, F_e is an element vector, and $\hat{q}$ is an applied flux and n is the outward point normal to the boundary $\partial\Omega$. Γ_e refers to the elements lying on the domain boundaries.

10.1002/2014GC005450

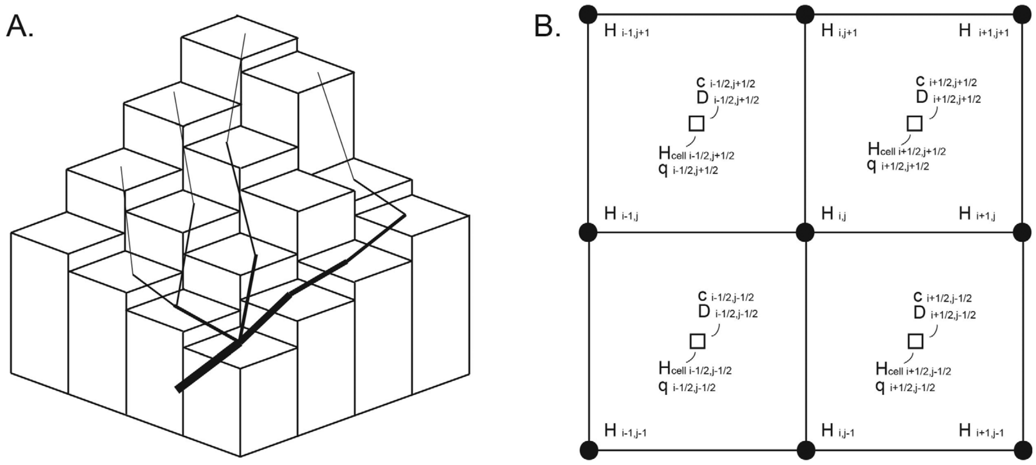

Figure 1. (A) Schematic representation of the drainage network, where each donor has only one receiver and (B) discretization used for the surface processes model. The diffusion coefficient is defined at the element centroid.

Contrary to *Simpson and Schlunegger* [2003], who used a continuum approach to solve equation (9), we compute the water discharge, q in equation (9) using a discrete routing algorithm [e.g., *Chase*, 1992]. This method consists in routing both sediment and water down the computed drainage network between nearest discrete neighbors from the highest to the lowest elevation (Figure 1A). Our finite element mesh is defined via a structured mesh of quadrilateral elements, where the effective diffusion coefficient $cq^m + k$, and the individual quantities c, q, and k are defined at the element centroid (Figure 1B). Given the location where the diffusion coefficient is defined, the fluid discharge was computed using the average element height, in combination with the D8 algorithm [*O'Callaghan and Mark*, 1984]. This algorithm can be computed in a simple and recursive manner with the following procedure:

1. Find the lowest neighbor of every cell (which can also be itself) and store its index in an array (ind_neigh). Store the elevation (H_{cell}) and the index of every cell (ind_{cell}) in two other arrays.

2. Sort the three arrays (ind_neigh, H_{cell}, ind_{cell}) from highest to lowest elevation (using H_{cell}).

3. Create an array that stores the amount of rain attributed to each cell (which can be spatially variable).

4. Starting from the highest cell, transfer the water of the current cell (donor) to its neighbor with the lowest height (receiver).

Once all cells have been processed in this manner, we know the water flux q ($m^2\ s^{-1}$) at every cell, which is then used to compute the effective diffusivity of the cell, according to equation (7). We note that the D8 algorithm suffers from a grid dependency, which can however be masked using high resolution [*Braun and Willett*, 2013], an irregular spatial grid [*Braun and Sambridge*, 1997] and/or by adding a small component of diffusion [*Perron et al*., 2008].

Discretizing equation (11), using an implicit time stepping algorithm gives:

$$M\left(\frac{H^{n+1} - H^n}{\Delta t}\right) + KH^{n+1} = F^n, \tag{15}$$

where K, M are the global stiffness matrices associated with K_e, M_e; H, F are the global vectors associated with the element vectors H_e, F_e; Δt is the time step; K is the diffusion operator; H^{n+1} is the new elevation (i.e., solution); and H^n is the elevation known at the previous time step. The drainage network, and consequently K are defined using the elevation known at the previous time step, H^n. Equation (15) is solved using the Krylov method FGMRES [*Saad*, 2003] with a diagonal preconditioner (Jacobi). Due to the use of a sorting algorithm in the steepest descent algorithm, which is complex to parallelize, the SPM is currently serial (i.e., it can only run on one processor).

10.1002/2014GC005450

2.3. Coupling Between the Mechanical and Surface Process Model

Here we outline the procedure adopted to couple the mechanical model (MM) with the surface process model (SPM). Quantities defined by the mechanical model, and the erosion surface used by the SPM will be referred as XX^t_{MM} and XX^t_{SPM}, respectively, with the prefix XX, representing physical parameter such as elevation (H), velocity (V), or pressure (P). The ratio between the element resolution of the erosion surface (which has a finer mesh) and the internal free surface (which has a coarse mesh) is denoted by ResolutionFactorX and ResolutionFactorY, in *x* and *y* directions, respectively. The following pseudoalgorithm illustrates how we coupled both models:

1. Initialize both H_{MM} and H_{SPM}. H_{SPM} is defined on processor 0 (rank 0) at the same level as the internal free surface, whereas the H_{MM} is fully parallel.

2. Solve the discrete Stokes equations for V^t_{MM} and P^t_{MM}.

3. Compute Δt_{MM}.

4. Copy the H^t_{MM} and V^t_{MM} (the velocity at the internal free surface) from all processors to rank 0 (as the SPM is serial).

5. Interpolate V^t_{MM}, defined on rank 0 to V^t_{SPM}, using bilinear interpolation.

6. Advect H^t_{SPM} using V^t_{SPM}: $H^t_{SPM} = H^t_{SPM} + \Delta t_{MM} V^t_{SPM}$.

7. Remesh the deformed H^t_{SPM} onto a nondeformed mesh of the same resolution.

8. Set $t_{SPM} = 0$.

9. Define the time step for the SPM, such as $\Delta t_{SPM} = \gamma \Delta t_{MM}$, with $\gamma < 1$.

10. Solve equation (15) with Δt_{SPM}.

11. Update time: $t_{SPM} = t_{SPM} + \Delta t_{SPM}$.

12. Go to step 10 and repeat until $t_{SPM} = \Delta t_{MM}$.

13. Interpolate $H^{t+t\_SPM}_{SPM}$ back to MM on rank 0, defining $H^{t+\Delta t}_{MM}$.

14. Distribute $H^{t+\Delta t}_{MM}$ on several processors.

15. Update lithology.

16. Update time, $t = t + \Delta t_{MM}$.

17. Go to step 2.

The interpolation from V_{MM} to V_{SPM} is performed using bilinear interpolation. The interpolation from H_{MM} to H_{SPM} is performed considering for each element of the H_{MM}, the associated nodes on the H_{SPM} using both ResolutionFactorX and ResolutionFactorY. This interpolation is done using an arithmetic average, such as:

$$H_{MM}(i,j) = \frac{\sum_{ii=1}^{n} H_{SPM}(ii)}{n},$$

where i and j are the indexes of the nodes of the S_{MM} and ii is the indexes of the nodes of the S_{SPM}, associated to the considered area (Ω) of each $H_{MM}(i, j)$. For each $H_{MM}(i, j)$, Ω is defined by the first surrounding elements (i.e., four within the mesh, two at the boundaries, and one at the corners). As velocities are typically smooth, we found this approach to work better than other approaches, which for example advect the coarse grid and interpolate differences in elevation back to finite erosion model.

3. Model Setup and Boundary Conditions

The style of deformation in fold of and thrust belts is mainly controlled by the number and the type of décollement [*Ruh et al.*, 2012]. It was recently demonstrated using 2-D numerical simulations [*Yamato et al.*, 2011] that considering a detailed stratigraphic column above a level of detachment can strongly influence the deformation style occurring in fold and thrust belts (i.e., dominated by folding rather than faulting). In this study, we focus on the fold-and-thrust belt systems in which the deformation is dominated by folds, e.g., Zagros Simply Folded Belt (ZFB) in the Fars Province, Iran [*Colman-Sadd*, 1978; *Mouthereau et al.*, 2012;

Yamato et al., 2011]. Therefore, and for computational efficiency, we use linear viscous constitutive laws, and do not consider plasticity (which implies that we cannot model faults). As a consequence, even if this study does not primarily aim to model the Zagros Mountains, but rather the relative influence of two general processes (folding and erosion), we use the ZFB as our first and most robust natural analogue for our mechanical model, as it is a folding-dominated fold-and thrust-belts [*Ruh et al*., 2012; *Yamato et al*., 2011]. The effect of changing the rheology of the overburden on folding dynamics and fold pattern formation is addressed in a separate study [*Fernandez and Kaus*, 2014].

Here we examine a multilayer setup in which folding is affected by gravity in a domain of size 100 × 100 × 10 km. The model consists of eight mechanical layers. A lower detachment (or salt layer) is used at the base of the model, while the stratigraphic column is built of seven alternating weak and competent layers (see Figure 2 and Table 2). The choice of height layers is based on the lithostratigraphic column of the Fars Province and the findings discussed in *Yamato et al*. [2011]. In order to observe the characteristic fold wavelength and deformation style (folding rather than thrusting) of the Zagros, the model employs intermediate weak layers within the sediment cover. As we did not consider any plasticity, we could have used a model with fewer layers, but this would have result in different fold growth rates. We employ the same thickness for all layers to ensure that the weak layers are numerically well resolved, while at the same time similar structures as in the Zagros. Previous work that employ the observed stratigraphic column in combination with frictional plastic rheologies resulted in crustal-scale folding with similar growth rate curves as employed here [*Yamato et al*., 2011]. Random perturbations are applied at the interface between the salt layer and the overburden. Above the eight mechanical layers, we fill the domain with "sticky-air" material. The "sticky air" is used in combination with an internal free surface in order to approximate a true free surface [*Crameri et al*., 2012]. At the interface between the sedimentary cover and the "sticky-air" layer a regional slope of angle β is defined, which is required for the SPM to allow the development of a dense drainage network. On all boundaries, we impose a zero shear stress (e.g., σ_{ij} $t_j = 0$, where t_j is an unit vector tangent to the boundary). A Dirichlet boundary condition is applied in the *y* direction as $V_y = \dot{\varepsilon}_{BG} y$, with $\dot{\varepsilon}_{BG}$ being the background strain rate, whereas all other boundaries have zero normal velocities. As the coordinate y is updated during the simulations, the velocity applied on the side of the model changes with time.

In most calculations, we present, the mechanical model used a resolution of 32 × 32 × 80 elements. In order to test how robust our findings are from these small-scale models, we additionally performed some simulations with a higher resolution of 256 × 128 × 200 elements, using 1024 cores, on a domain of 240 × 120 × 10 km, using the same model setup with seven alternating weak and strong layers, overlying a lower detachment (salt). The salt and the weak layers have a viscosity of 10^{19} Pa s, while the strong layer have a viscosity of 10^{22} Pa s. The viscosity of the salt has been chosen accordingly to literature, where 10^{19} appears to be a common value [*Mukherjee et al*., 2010]. We used a high viscosity contrast in order to have dominant wavelengths corresponding to lithospheric folds (i.e., in the order of 10 km). The resulting dominant wavelengths and growth rates for this setup are in the range of those for the Zagros Folded Belt [*Mouthereau et al*., 2007; *Yamato et al*., 2011], which has been chosen as a natural analogue for this study.

For the surface processes model, the boundaries normal to the direction of compression are defined as the base levels and are therefore kept at constant elevation during the SPM updates. The flux $\hat{q}$, defined in equation (14), is set to zero on the other boundaries. The topography is updated after every mechanical time step, implying that the base level is only kept at constant elevation while the SPM is run, between two mechanical time steps. The resolution of the surface processes mesh is usually 10 times higher than the one used for the tectonic model (i.e., 320 × 320 cells). Due to the use of a D8 algorithm, the spatial resolution used within the SPM should be on the order of 100 m if one wants to capture both hillslopes and fluvial processes. A number of preliminary tests were performed to investigate how the resolution factor between both codes influences the results, and showed that little differences in the results occur for resolution factors lower or equal to 10.

4. Model Results

In order to determine the influence of surface processes on the three-dimensional development of folds, a series of simulations were performed with different background strain rates, and with different erosional regimes (i.e., varying the regional slope β, the fluvial incision, and/or the hillslope diffusion). For each

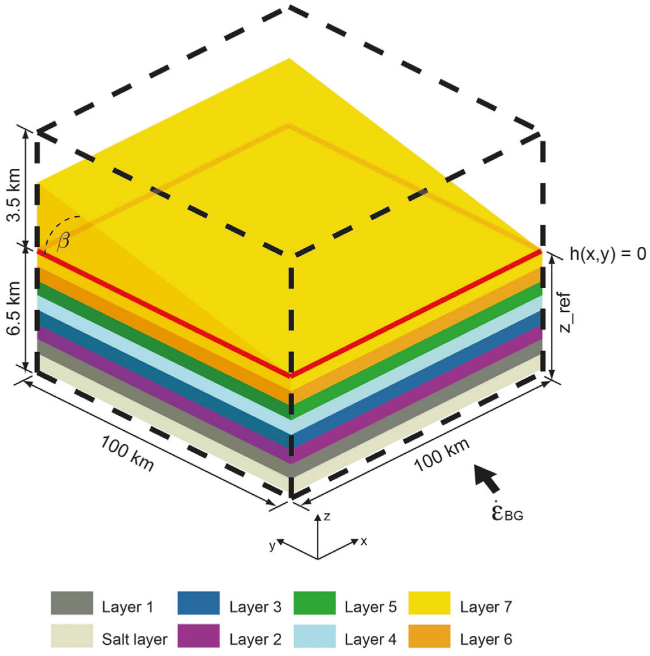

Figure 2. Geometry (not to scale) of the multilayer folding experiments used in this study. The model consists of seven layers, with alternating weak and strong viscosities (see Table 2 for parameters). Above layer 7, we fill the remainder of the model domain (dashed lines) with "sticky air." The red plane represents the reference level (z_ref) with which we define the topographic elevation, h(x,y) = z_model-z_ref. For clarity, the *z* axis has been exaggerated. See text for further details about boundary conditions and physical parameters.

simulation, only one parameter was modified to better understand their relative influence. Table 3 summarizes the values for the physical parameters used in the different simulations.

4.1. Simultaneous *D*evelopment of *Folds and Drainage Network*

We first performed simulations in which the drainage network was developing at the same time as the folding and compare the results with those of a model without surface processes.

4.1.1. Deformation in the Absence of Surface Processes

Figure 3A shows the three-dimensional evolution through time of a model without surface processes, with a background strain rate of 10^{-14} s^{-1}. In this case, the folding pattern consists of several randomly distributed embryonic fold segments with a rather high aspect ratio. With increasing shortening, these fold segments grow laterally, forming doubly plunging en-échelon folds that eventually link into a long train of folds in a quasi-cylindrical manner. The end result consists of an array of three long train folds with a triple linkage on fold 3 (Figure 3A, shortening rate 27.5%). Fold 2, in the middle of the box, results in the linkage of en-échelon small segments, while fold 1, developing at the border of the box can be considered as cylindrical. The amount of shortening, Δy, needed to initiate folding is around 15% and is defined as $\Delta y = (L_0 - L)/L_0$, with L the length of the model in the y-direction at the considered time and L_0 the initial length.

4.1.2. Effect of Erosion

The same model with the same random noise at the salt-sediment interface but with erosional processes shows few differences: the fold morphology is sharper and the amplitude between the crest of the anticline and the syncline is reduced due to sedimentation in the syncline. The topography is modified but the fold pattern does not change much. However, the fold growth is slightly enhanced and the small randomly distributed segments link earlier (Figure 3B). In order to test the effects of erosion in a systematic manner, we performed a set of simulations with the same background strain rate and random noise at both the salt-sediment interface and the erosion surface, but with a different regional slope and/or erosion parameters (experiments 2–9). Map views of the upper surface models, representing the topographic elevation, show

Table 2. Physical Parameters Used for the Mechanical Model

Layer	Description	Thickness (m)	Density (kg m^{-3})	Viscosity (Pa s)
8	Sticky air	3500	0	10^{17}
7	Overburden	500	2700	10^{23}
6	Overburden	500	2700	10^{21}
5	Overburden	500	2700	10^{23}
4	Overburden	500	2700	10^{21}
3	Overburden	500	2700	10^{23}
2	Overburden	500	2700	10^{21}
1	Overburden	500	2700	10^{23}
0	Salt layer	3000	2200	10^{19}

Table 3. Physical Parameters Used for the Surface Processes Model in the Different Simulations

Simulation	Description	n	c	k	β	ε_{yy}	h_0
Experiment 1	No erosion, $\beta = 0$					10^{-14}	0
Experiment 2	Low to medium erosion, $\beta = 0$	2	10	10^{-10}	0	10^{-14}	5
Experiment 3	High to intensive erosion, $\beta = 0$	2	500	10^{-09}	0	10^{-14}	5
Experiment 4	No erosion, $\beta = 0.1\%$	2	0	10^{-31}	0.1	10^{-14}	5
Experiment 5	Low to medium erosion, $\beta = 0.1\%$	2	10	10^{-10}	0.1	10^{-14}	5
Experiment 6	High to intensive erosion, $\beta = 0.1\%$	2	500	10^{-09}	0.1	10^{-14}	5
Experiment 7	No erosion, $\beta = 0.2\%$	2	0	10^{-31}	0.2	10^{-14}	5
Experiment 8	Low to medium erosion, $\beta = 0.2\%$	2	10	10^{-10}	0.2	10^{-14}	5
Experiment 9	High to intensive erosion, $\beta = 0.2\%$	2	500	10^{-09}	0.2	10^{-14}	5
Experiment 10	Low to medium erosion, $\beta = 0.1\%$	2	10	10^{-10}	0.1	10^{-15}	5
Experiment 11	High to intensive erosion, $\beta = 0.1\%$	2	500	10^{-09}	0.1	10^{-15}	5
Experiment 12	Low to medium erosion, $\beta = 0.2\%$	2	10	10^{-10}	0.2	10^{-15}	5
Experiment 13	High to intensive erosion, $\beta = 0.2\%$	2	500	10^{-09}	0.2	10^{-15}	5
Experiment 14	Medium to high erosion, $\beta = 0.042\%$	2	50	10^{-10}	0.042	10^{-15}	0.5
Experiment 15	Medium to high erosion, $\beta = 0.33\%$	2	50	10^{-10}	0.33	10^{-15}	0.5
Experiment 16	Late folding, $\beta = 0.2\%$	2	10	10^{-10}	0.2	10^{-14}	5

that to first order, erosion does not seem to strongly control the wavelength, the location, or the pattern of folds (Figure 4).

To distinguish the effect of surface processes from that of a nonzero initial topography, we ran models in which the fluvial incision was set to zero and the hillslope diffusion to a very low value (10^{-31}), essentially eliminating surface processes. When an initial slope is added to the model, the fold pattern is slightly modified. The folds show a higher degree of cylindricity and higher amplifications for the same amounts of shortening (e.g., compare Figure 4, experiment 1 and Figure 4, experiments 4 and 7, see also Figure 5). Also buckling initiation, lateral fold propagation, and linkage occur earlier ($\approx$12%). The isolated fold segments, at the beginning of the simulations, become more linear with increasing slope. Increasing the efficiency of fluvial incision (by increasing *c*), on the other hand, does not have a first-order effect on the pattern of folds,

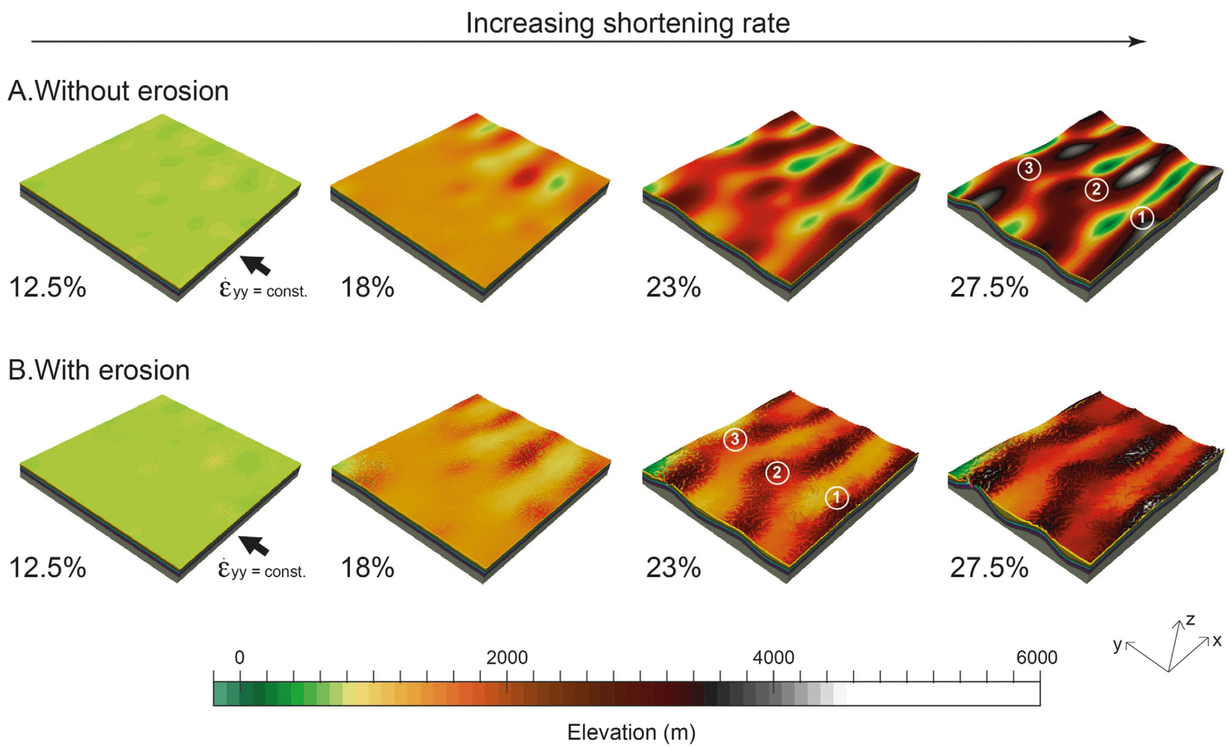

Figure 3. Three-dimensional evolution for (A) a simulation without erosion and (B) a simulation where surface processes are present. Model parameters used to relate experiments 1 and 8, respectively. The same random noise at the salt-sediment interface was applied in both cases.

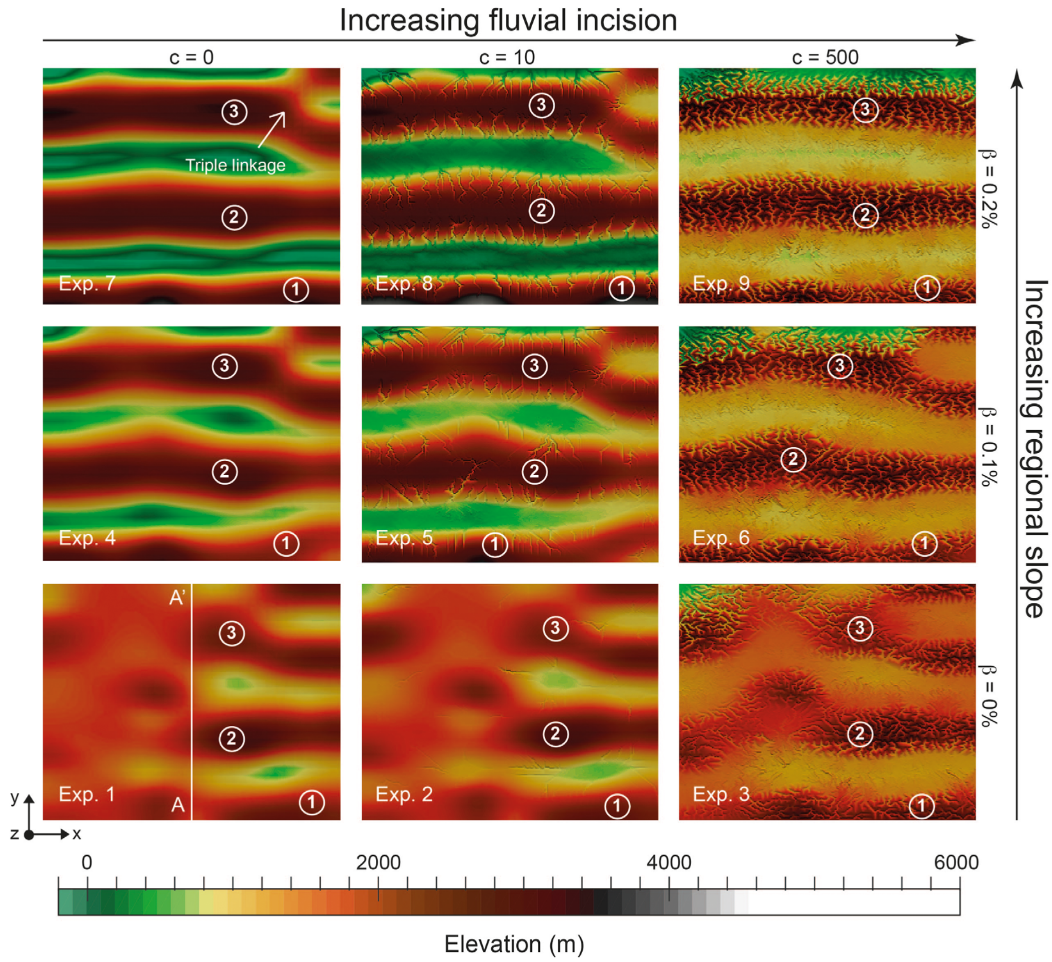

Figure 4. Model surface topographies for different erosional regimes, taken after approximately 20% of shortening. Elevation is plotted with respect to a reference level of 6.5 km from the model base, which corresponds to the interface between sticky air and the uppermost layer when no slope is employed (red square in Figure 2).

although the synclines become increasingly filled with eroded sediments. Maximum topographies are of the same order of magnitude in both cases. However, some small differences in the fold pattern can be noticed. For example, the triple linkage on fold 3, in experiments 7 and 8, has disappeared in experiment 9, under high to intensive erosion.

In order to see how surface processes affect exhumation and fold growth, we present a few horizontal cross sections of the lithology at the reference level of 6.5 km, at the end of the simulations (Figure 6). Results show that erosion amplifies the fold growth and therefore deeper layers are exhumed faster (compare, for example, experiment 9 with experiment 8, or experiment 3 with experiment 2, in Figure 6). In a next set of experiments (experiments 10–13), we employ a lower background strain rate of 10^{-15} (Figures 7 and 8), in order to test cases when the erosion characteristic time scale is comparable to, or significantly larger than the tectonic characteristic time scales. The initial random noise is the same as in the previous models. Results generally support the previous findings that erosion increases the fold growth and exhumation rates, but does not affect the folding pattern (Figures 5 and 7). However, if we compare the horizontal sections in Figures 6 and 8, we see that when applying lower background strain rates, deeper lithologies are found at the same reference level. This indicates that exhumation of rocks is more pronounced for models with lower background strain rates, where the erosion characteristic time scale is comparable to or larger than the tectonic characteristic time scale, suggesting that erosion enhances exhumation.

In order to study the lateral interactions between the fold and thrust belt and to have more three-dimensional arrays of folds, we performed a set of high-resolution simulations with a larger domain and

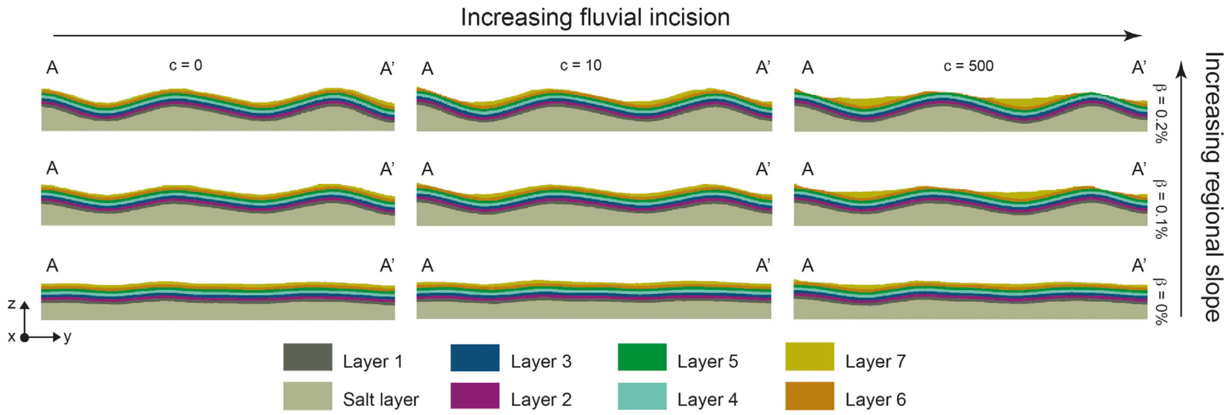

Figure 5. Vertical cross sections for different erosional regimes, taken orthogonal to the *x* axis and in the middle of the *y* axis. The section AA′ is shown in white in Figure 4.

background strain rate of 10^{-14}. Erosional parameters are given in Table 3, and the mechanical parameters were mentioned above in section 3. The overall results are similar to our previous findings. When the regional slope is steeper, the folds present larger aspect ratios and a higher degree of cylindricity (Figure 9). In the case of the higher regional slope, the folds develop first at the lower and upper boundaries. During compression and development of long anticlines at the lower boundary, the river network which was previously transverse, is progressively deflected by the growing structures with local reversion of rivers. This results in a discontinuity of the drainage network at large scale, and to its restriction to local basins that formed between the anticlines. We see as well that increasing the regional slope enhances the efficiency of the erosion and allows a faster development of the drainage network (compare regional slope 0.04% and 0.33% after 3% of shortening in Figure 9).

Running higher-resolution models also allow us to confirm the validity of our previous low-resolution models. Indeed in these low-resolution models, the location of folds as well as the development of folds at both upper and lower boundaries with increasing the regional slope could be debated and inferred to boundaries effects. However, we observed similar behavior in our high-resolution models. The location of folds is mainly controlled by the initial random noise at the salt-sediment interface, consistent with previous findings [*Fernandez and Kaus*, 2014; *Schmid et al.*, 2008].

Contrary to previous studies, which demonstrated the influence of sedimentation on fold wavelength [*Simpson*, 2004c] or on the external development of fold and thrust belts [*Fillon et al.*, 2013], sedimentation does not seem to have much effects on the fold patterns in our simulations. Its effect is rather secondary and consists in amplifying the fold growth rate by loading of the synclines (i.e., gravity).

4.2. Effect of Preexisting Drainage Network

In order to better understand whether erosion controls the folding pattern, or whether erosion has a more indirect effect by modifying the initial random perturbation at the surface, we performed several tests in which the coupling with the mechanical model was activated only after a drainage network was already developed. We used the same mechanical and erosional parameters as for experiment 8 (Table 3). The upper surface of the model is exposed to the surface processes model for ca. 1 Ma, while the mechanical code was not activated. After this time, a river network formed with changes in elevation on the order of 100 m between the river valleys and adjacent mountains. As such, it thus adds additional perturbations to the initial model, which are of similar order of magnitude as the initially imposed random noise at the salt-sediment interface. Results show that the presence of a drainage network before tectonic deformation has a strong effect on the pattern and development of folds. The amount of shortening needed to initiate folding is strongly reduced ($<$10%) if an initial drainage network is present, and the folding pattern presents some slight differences (see vertical cross sections in Figure 10 and topography evolution in Figure 11).

In most previously discussed simulations (low-resolution models), three quasi-cylindrical folds formed due to lateral growth of randomly distributed embryonic fold segments. All folds had similar (low) amplitude,

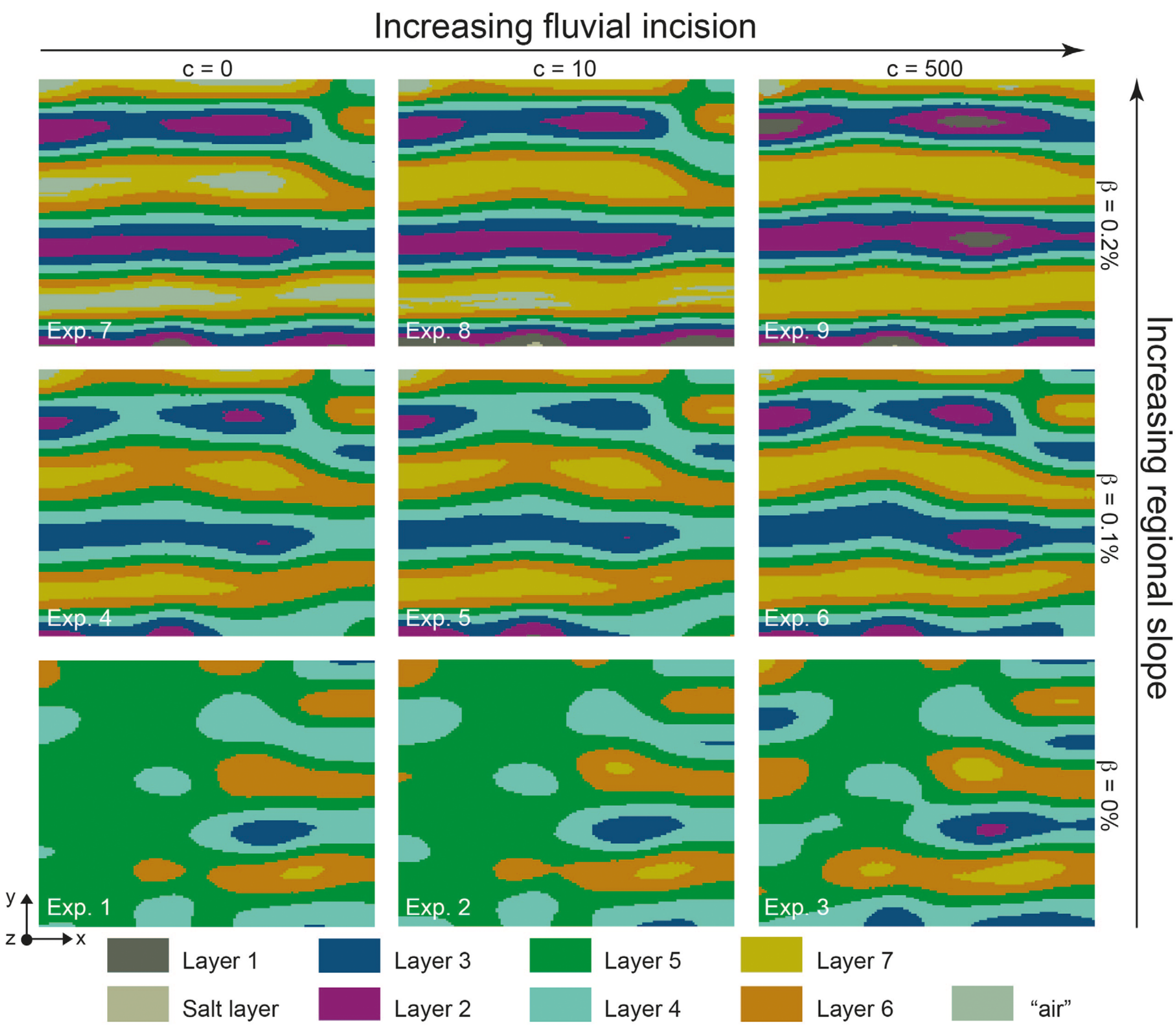

Figure 6. Horizontal cross sections for different erosional regimes, taken at the reference level and after approximately 20% of shortening.

wavelength, and low aspect ratio (Figure 11A), and the top of the anticlines was at the same altitude. When a preexisting drainage network is present, folds 1 and 3 (Figure 11B) show much higher amplitude and lower aspect ratio, for a same amount of shortening. In contrast, fold 2 (which develops in the middle of the domain) shows very little amplitude and a higher aspect ratio compared to folds 1 and 3 (Figures 10 and 11). It also shows lower topographic height than the two others. The triple linkage that occurred on fold 3 in the previous simulations is no longer present. Folds 1 and 3 are true cylindrical folds. Fold 2 represents a slightly more complex geometry and seems to consist of both lateral propagation and integration of another segments (left side), which resemble like a tentative of triple linkage that would have failed. The growth rate, and as consequence, the exhumation rate are much more enhanced on both sides of the domain, compared to the middle (Figure 12).

5. Discussion

5.1. General Observations

Our results are in good agreement with previous two-dimensional models performed at larger length scales [*Avouac and Burov*, 1996; *Beaumont et al.*, 1992; *Kaus et al.*, 2008; *Willett*, 1999], as well as with analogue models of accretionary wedges [*Konstantinovskaia and Malavieille*, 2005], which have demonstrated

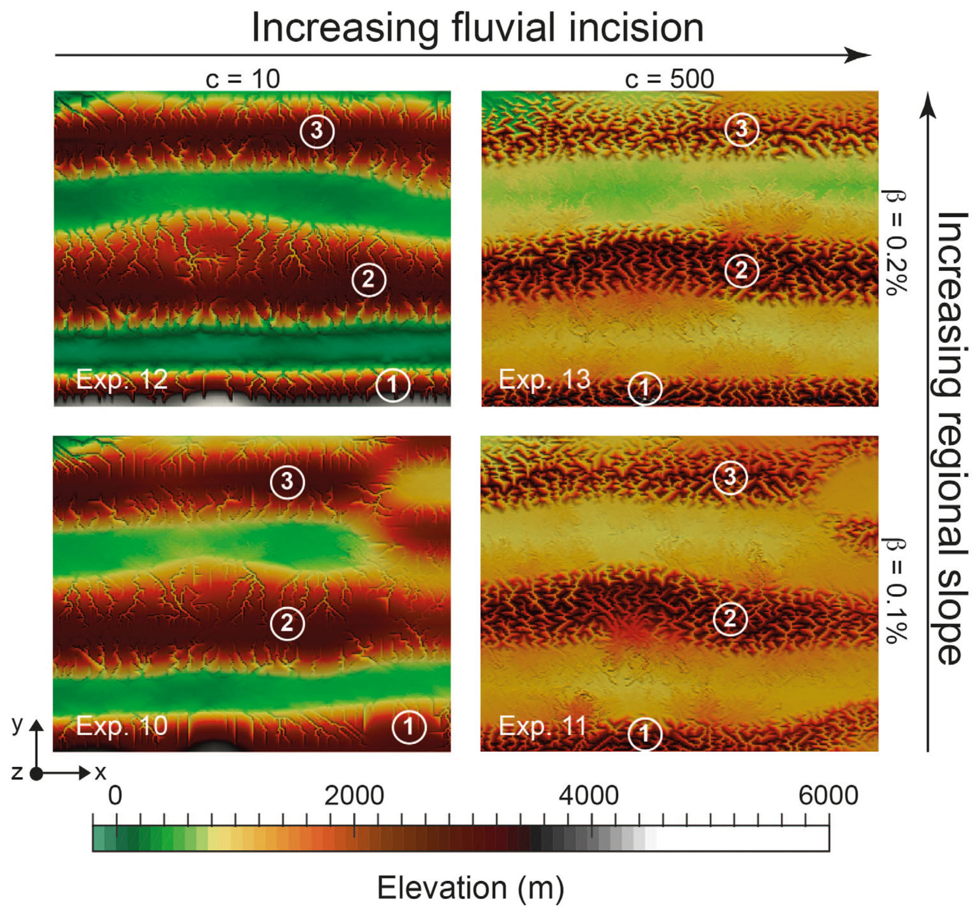

Figure 7. Model surface topographies for different erosional regimes, taken after approximately 20% of shortening. A strain rate of 10^{-15} was considered.

that erosion has a strong effect on the deformation. Erosion mainly enhances the relief, and thus enables the exhumation of deeper rocks [*Burbank*, 2002; *Willett*, 1999]. In this study, the isostatic compensation is not taken into account as we focus on crustal-scale models, but erosion and deposition still have the capacity to enhance the exhumation rate by unloading of anticlines and loading of synclines. The resulting mass redistribution amplifies folding by gravity [see also *Burg et al*., 2004]. It also reduces the amount of shortening needed to initiate folding. Below, we discuss the effects of a preexisting drainage network as well as those caused by surface processes and a regional slope.

5.1.1. Effects of Surface Processes and Regional Slope

If no regional slope is applied to the model, surface processes do not strongly influence the deformation, and have only a visible effect in enhancing the growth rate when high to intensive fluvial erosion is prescribed (Figures 4 and 6, experiment 3). Specifically, in order to be able to incise and remove sediments from the model, a minimum relief needs to be present, which usually occurs only after the layers started to buckle. During the phase of thickening, the entire surface is uniformly uplifted and stays rather flat, which does not allow the drainage network to develop. Increasing the steepness of the regional slope has two major effects on the deformation pattern. First, it increases the efficiency of the drainage network, which removes more material in the first stages of deformation (Figure 9). This results in an increase of the fold growth and a diminution of the amount of shortening to initiate buckling. The second and strongest effect is that when a regional slope is employed, spatial variations in thickness of the uppermost layer are introduced within the model. When the surface processes model is activated, two types of perturbations are present within the model. The first one is the random noise used in the SPM to initiate incision of rivers, while the second is the thickness variations in the uppermost layer introduced by the

10.1002/2014GC005450

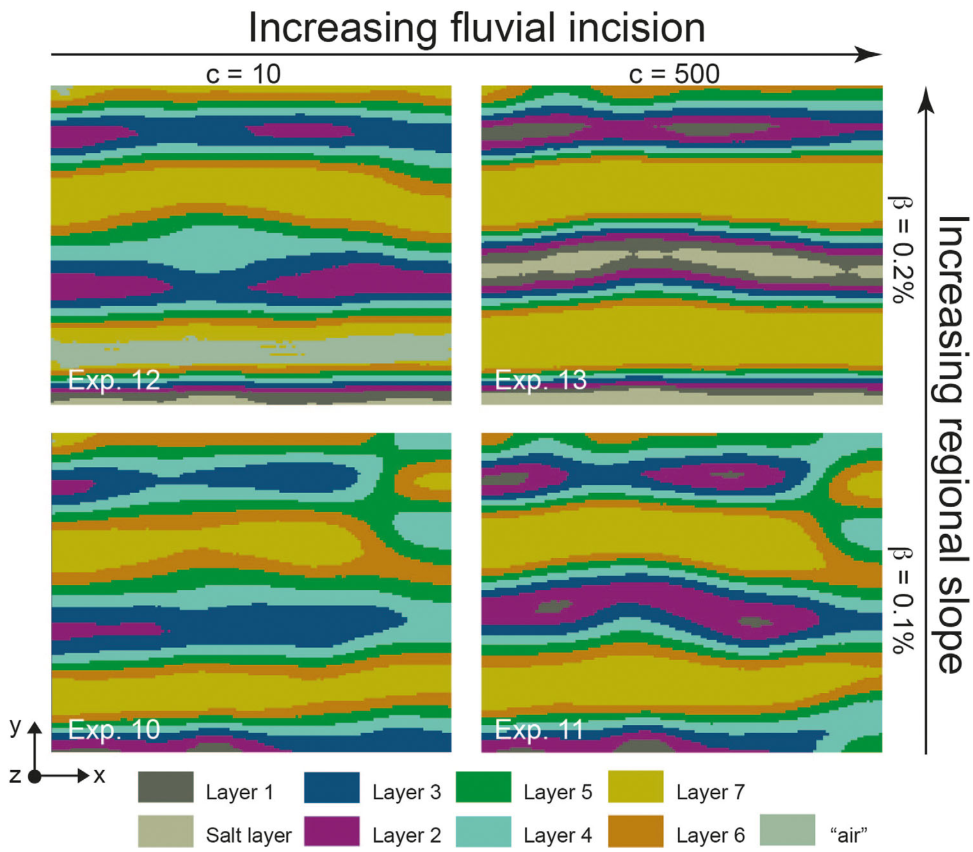

Figure 8. Horizontal cross sections for different erosional regimes, taken at the reference level and after approximately 20% of shortening. A strain rate of 10^{-15} was considered.

regional slope. The 5 m of random noise in the SPM can be considered as negligible compared to both the 150 m of the background perturbation in the mechanical code, and the ca. 300 m of spatial resolution. The thickness variations introduced by the regional slope, in contrary, are of the same order of magnitude as the background perturbation, and have the potential to modify the fold growth rate. Folding of a single viscous embedded layer in a matrix is controlled by the viscosity contrast between the layer and the matrix, the layer thickness and the initial perturbation prescribed at the layer interface [*Biot*, 1961; *Fletcher*, 1991, 1995; *Ramberg*, 1964]. Higher amplification of small wavelengths is associated with smaller layer thicknesses when an out of phase perturbation is applied to the layer [*Mancktelow*, 2001]. In the case of a multilayer folding, the instability can extend to the entire stack [*Cobbold*, 1976] and the viscous layers behavior (as individual layers or as one single layer) depends on the interlayer spacing [*Schmid and Podladchikov*, 2006]. Also fold amplification rates and dominant wavelengths selection are controlled by the ratio between the salt and sediment cover thickness [*Schmalholz et al*., 2002]. Therefore, when a regional slope is used, it introduces a wedge-shaped geometry to the model, which has two main effects. The first is to modify the initial perturbation by changing the ratio between the initial random perturbation and the layer thickness, resulting in amplification of the growth rate in the thinnest parts of the model. The second is to amplify the cylindrical component of the dominant wavelength [*Fletcher*, 1995], resulting in a more linear distribution of the embryonic fold segments. The most likely reason for this is that the initial wedge-shaped geometry tries to flatten due to gravity (and reach isostatic equilibrium) and therefore flows on the weaker underlying salt layer. This induces a two-dimensional flow pattern, and as a result the first folds that form are linear and in the vicinity of the upper and lower boundaries. However the variations in thickness are relatively low and smooth in most models (i.e., the regional slope is <0.33% and spatial variations in the directions normal to compression is not considered) compared to the physical model, and even if the fold growth can be affected, the wavelength of the folds does not vary significantly as a result of this.

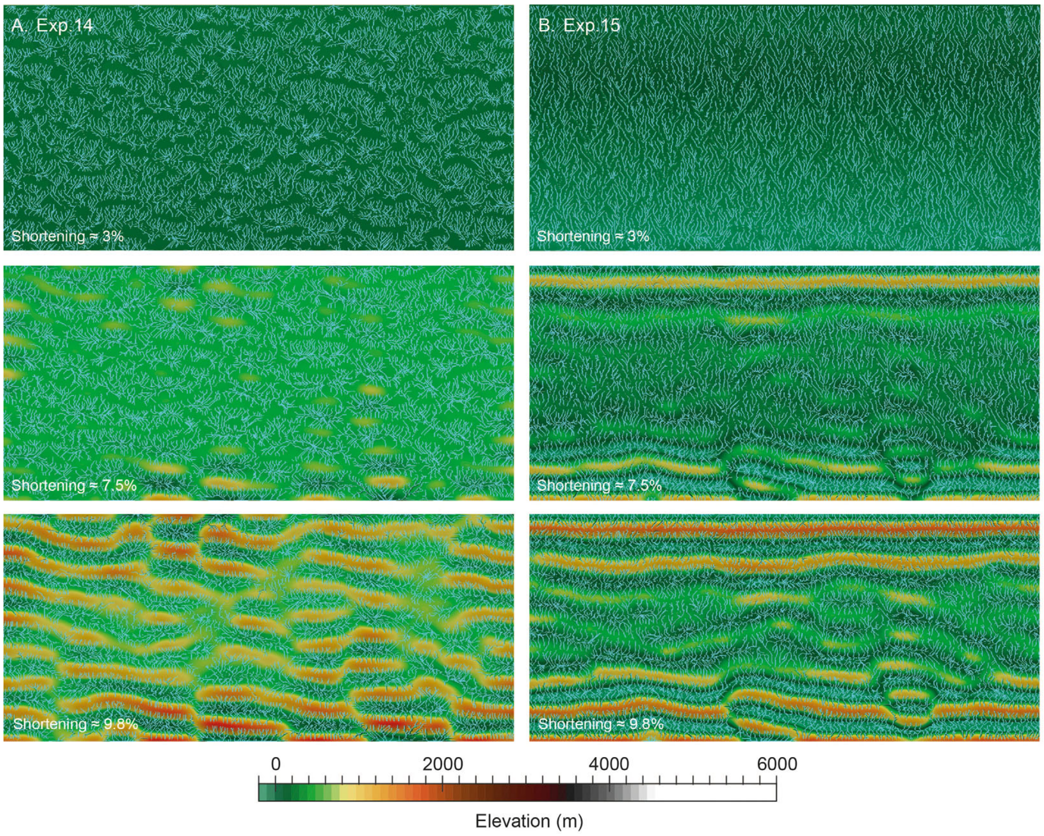

Figure 9. Evolution of the topographic elevation with increasing shortening for a regional slope of (A) 0.04% and (B) 0.33%. The drainage network is shown in light blue.

5.1.2. Effects of the Presence of a Preexisting Drainage Network

In the case of a preexisting drainage network, the initial surface topography has been exposed to erosion such that a considerable amount of sediments have been removed. Simultaneously more roughness in the topography was introduced as a result of fluvial incision. There is thus an initial spatial variation in thickness in both x and y directions. As previously, higher fold amplifications would be expected in the thinnest part of the layer. In other words, folds will grow preferentially at the compression front and where the fluvial incision has been the deepest (i.e., in the upward part of the model). If at these locations, channels were at more or less the same elevation, folding growth rate would tend to be rather uniform, resulting in the development of a cylindrical fold. This is likely to be the case in numerical simulations where we consider a linear slope and a constant erodibility throughout the entire domain. Moreover, due to gravity the initial wedge-shaped geometry has the tendency to flatten, resulting in positive and negative vertical velocities at the lower and upper boundaries, respectively. The combined gravitational and erosional effects result in deformation that is localized to the two cylindrical folds on each sides of the model, limiting the growth of the structures in the middle part. This effect is more pronounced in the case of a preexisting drainage network, suggesting that erosion can also modify the fold growth rate locally. The initial exponential growth of the folds [*Biot*, 1961; *Fletcher*, 1991, 1995] would progressively decrease and stop when folds get locked [*Schmalholz and Podladchikov*, 2000], allowing the propagation of deformation and growth amplifications of the other structures.

To summarize, the results of our coupled 3-D mechanical and surface processes simulations have shown that whilst the primary control on the location of folds is determined by the initial random noise at the salt-overburden interface [see also *Schmid et al*., 2008], and the fold growth by the viscosity contrast between the layers and the initial amplitude of the random noise, surface processes can influence the dynamics of the folding process. While erosion tends to reduce the amount of shortening needed to initiate folding and

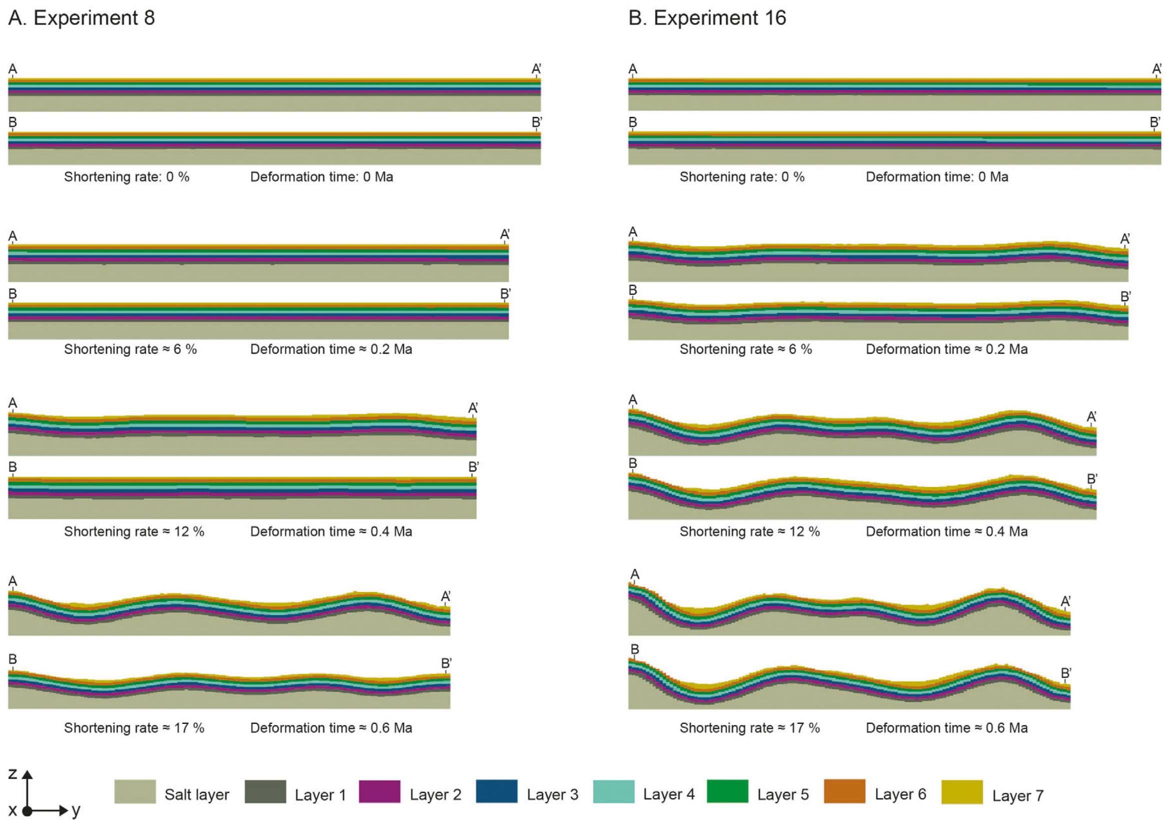

Figure 10. Temporal evolution of two vertical sections of the model, (A) for the case where the drainage network develops simultaneous with folding and (B) for the case where it was emplaced before folding starts. A preexisting drainage network enhances fold growth but does not result in significantly different fold wavelength.

to increase the exhumation rate, sedimentation in the synclines tends to amplify the fold growth rate by gravity. However, surfaces processes do not seem to influence the folding pattern within the fold and thrust belt, nor the location of folds. The main effect of surface processes is rather indirect and resides in its ability to create rough topography and therefore to amplify the background perturbation, which initiates the entire folding processes (i.e., due to the presence of an initial nonzero topography, considering either a regional slope or a preexisting drainage network).

5.2. Comparison With Previous Work

5.2.1. Comparison to Thin-Plate Models

The general observations that the ability of surface processes to influence deformation is mainly dependent on the regional slope β and the efficiency of surface processes with respect to tectonic uplift (i.e., ratio between erosion and deformation time scales) are similar to those of *Simpson* [2004a, 2004b]. However, the deformation pattern we observed in our models is quite different due to the use of a fully 3-D tectonic model.

When a thin-plate model is used [*Simpson*, 2004a, 2004b, 2004c], the folds are purely cylindrical for the case where no surface processes are applied, then evolve into en-échelon folds pattern and doubly plunging folds once the efficiency of the drainage network is increased (i.e., by increasing the regional slope or the fluvial incision). When a regional slope is considered, higher folds amplitude and buckling initiation occur near to the upper boundary (away from the compression front), which enhances the river incision, allowing the persistence of a transverse drainage network. The variations in thickness of the plate are likely to be of secondary importance.

In contrary, in our simulations, we consider a fully three-dimensional model of deformation (multilayer setup), where the number, the thickness variation and the spacing of the viscous layer would strongly influence the fold growth rate and the dominant wavelength selection [*Kaus and Schmalholz*, 2006;

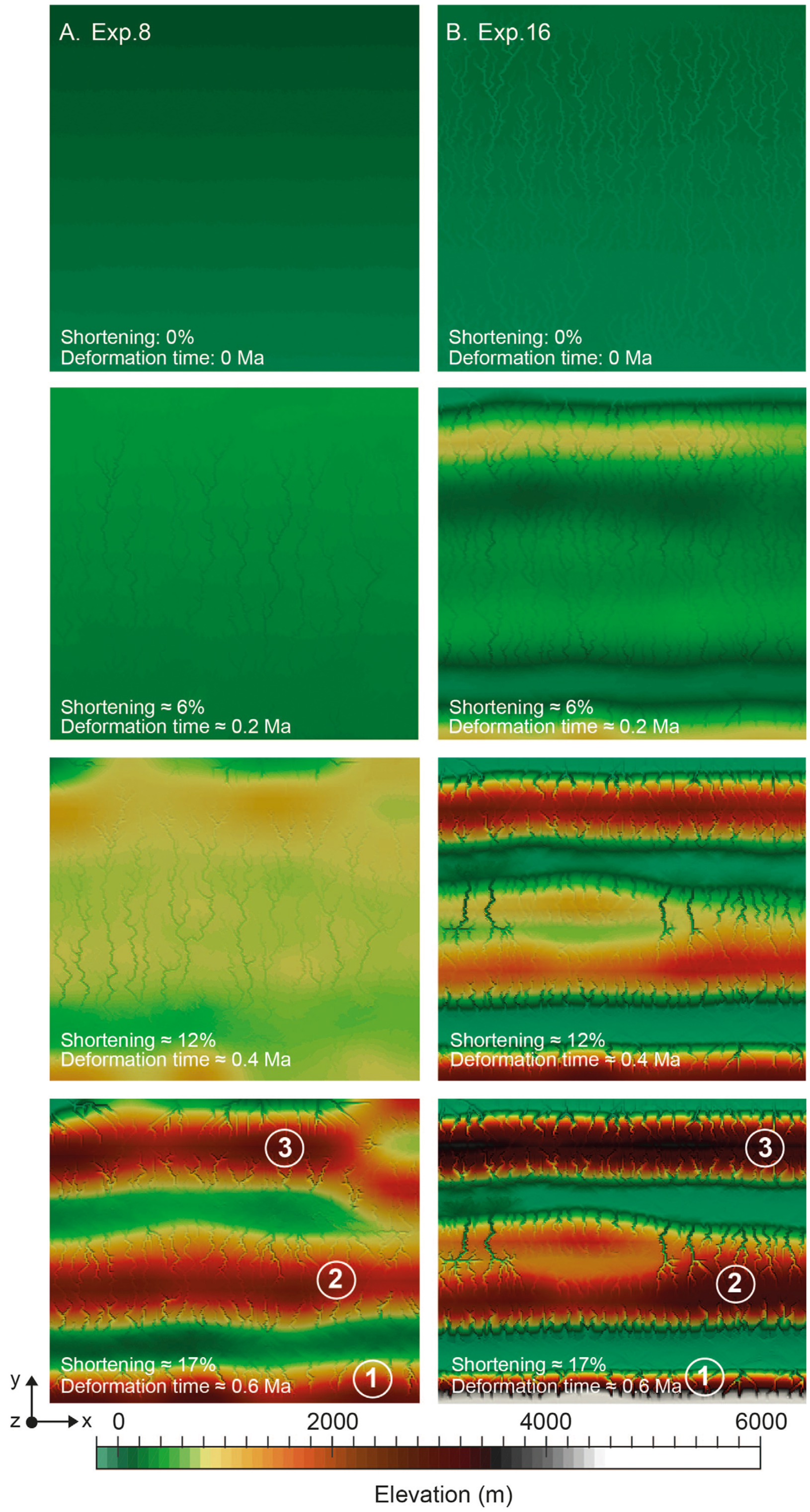

Figure 11. Evolution of the model surface topographies with increasing shortening rate, (A) for the case where the drainage network developed in the same time as folding and (B) for the case where it was emplaced before the folding.

Schmalholz et al., 2002; *Schmid and Podladchikov*, 2006]. As the results have shown, variations in thickness of the uppermost layer (in one or two directions) can greatly modify the fold pattern by increasing the cylindrical component of the dominant wavelength and the amplitude of the initial perturbation. With our

10.1002/2014GC005450

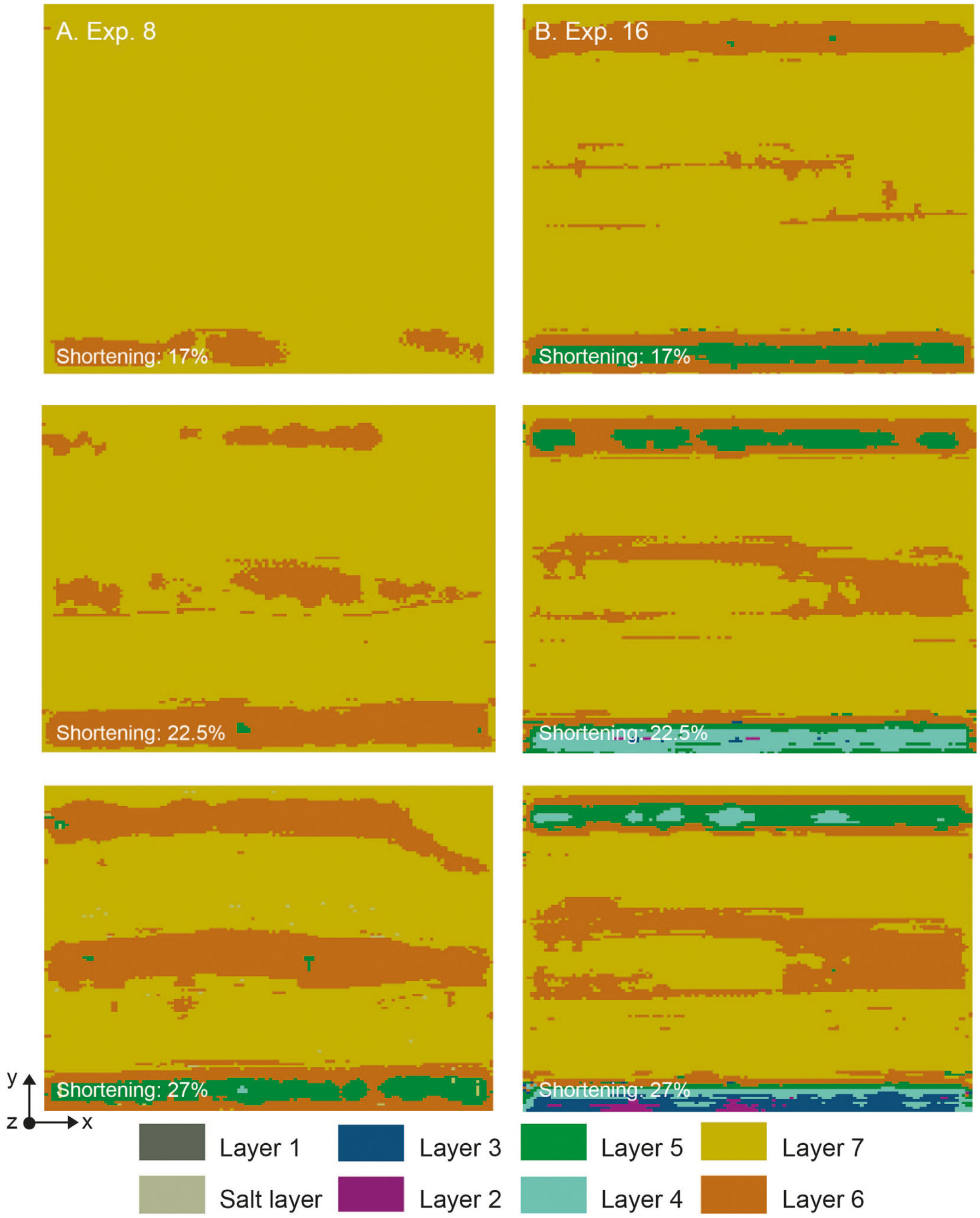

Figure 12. Exposed lithologies with increasing shortening rates (A) for the case where the drainage network developed in the same time as folding and (B) for the case where it was emplaced before folding.

model, folds develop as doubly plunging structures that link to form quasi-cylindrical long train folds even in a pure mechanical setup (no surface processes), and evolve toward "true" cylindrical folds while increasing the efficiency of surface processes. When a regional slope is considered, buckling occurs at the regional front where the sedimentary pile is thinner, resulting in a disconnection at large scale and local reversal of the drainage network. As a consequence, simple local drainage systems are now restricted to anticlines, and have lost their capacity to localize the deformation.

The difference in the folding patterns observed between *Simpson* [2004a] and our models are attributed to the fact that our 3-D models are sensitive to thickness variations, and the location of buckling onset, as well as its amplification. When buckling occurs at the upper boundary away from the compression front, the drainage network is still connected at large scale, while when it occurs at the compression front, rivers quickly loose their incision capacity and tend to be reversed. Thus, the capacity of surface processes to influence three-dimensional folding is related to the length scale over which sediment transport takes place [*Simpson*, 2004a] and is greatly depending on the temporal persistence of transverse drainage and a large-scale connectivity of the drainage network. Two other differences noticed between *Simpson* [2004a] and our models, which may explain why a transverse drainage network cannot be sustained throughout the growing structures, are:

1. The slope steepness is a factor of 10 lower in our simulations.

2. The amount of shortening needed to initiate buckling is higher in most of our simulations (low resolution), resulting in a general uplift of the entire model that decreases the river incision capacity.

In our numerical model, for the physical domain and viscosities considered, a regional slope of 1% is sufficient to localize deformation at the compression front, resulting in the development of a single, large amplitude cylindrical fold. In order to have an array of folds that are more similar to those observed in natural fold-and-thrust belt, we should therefore use smaller slopes. The observed differences in the amount of shortening required to initiate folding, between our simulations and thin-plate models, can be explained by the difference in the dominant growth rate that developed in the different models (i.e., thin-plate versus 3-D models).

5.2.2. Occurrence of River Incision at the Anticline Culmination

Another feature reported by *Simpson* [2004a, 2004b] and observed in nature [*Oberlander*, 1985], but which is not present in our simulations, is the occurrence of rivers cutting at the culmination of anticlines. The likely explanation is that the drainage network in our simulations is disconnected, and thus does not have the capacity to localize the deformation. Another possible explanation resides in the choice of the erosional parameters between the different lithologies. In order to explain transverse drainage in an orogen, *Oberlander* [1985] proposed a combined model of antecedence and superposition in a sequence containing resistant limestone formations separated by large amount of easily erodible flysch-like sedimentary rocks. In our simulations, we assumed a constant rainfall through time and space and prescribed the same erodibility for the different mechanical layers. Whilst this assumption is unlikely to be valid in nature, in this work, we focused on understanding the systematics of the coupled system. We also note that in general, the erosional parameters exhibit a high degree of variability and large uncertainties [*Braun*, 2006]. Thus, when using coupled models to understand the geomorphology of a specific region, those parameters are usually chosen arbitrary in order to fit a true landscape. Moreover, due to the difference of the characteristic time scales at which tectonic and surface processes occur, fully coupled models tend to use large time steps within the SPM (e.g., on the order of hundred years) and often assume a constant rainfall in space and time. As a consequence, sudden and catastrophic events such as flood due to high seasonal rain will not be captured. Such spontaneous rainfall events can however have a high incision potential, especially in desert conditions (e.g., Zagros or Makran, Iran), where the soil is not able to absorb the water, resulting in important river floods that can possibly cut through anticlines.

To summarize, we observed that in our simulations, a higher erosional efficiency results (e.g., steep slope and/or high fluvial incision) in a higher background perturbation and therefore in larger fold amplification velocities. Folding dominates over river incision and the drainage system is disconnected at large spatial scales. Surface processes would thus only have an influence in the exhumation rate and potentially, at local length scales, in the preservation of some structures such as the triple linkage of embryonic folds. However, the general three-dimensional fold pattern of the entire fold and thrust belt will not show much variations. In order to ensure long-range sediment transport, and to be able to see the potential influence on the fold pattern, the initial geometry, and boundary conditions of the model should be modified. A setup similar to *Ruh et al*. [2013] where the bottom sheet is pulled out below a rigid backstop, such as in analogue modeling [*Konstantinovskaia and Malavieille*, 2005] would be more appropriate to address this. With such a configuration, folds develop in sequence with the deformation front moving away from the rigid backstop.

5.3. Applications

Due to the choice of transport law and formulation of our surface processes model, together with the linear viscous rheology we have utilized, our model results can only be applied to orogens where the

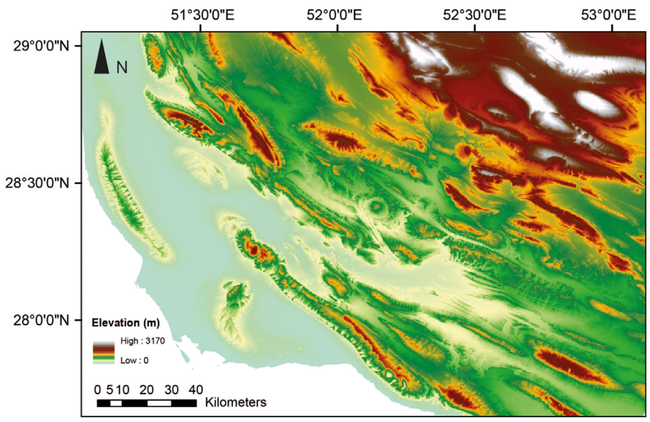

Figure 13. Digital elevation model of the Zagros Simply Folded Belt.

deformation style is dominated by folding, and where transport-limited conditions in rivers are dominant, such as the Zagros Folded Belt (ZFB) in Iran. The main outcomes of our simulations concerning the competition between folding and surface processes can certainly be applied to other natural folding-dominated systems as well, such as in the Folded Jura. Yet, the Zagros is an ideal application area, as previous work clearly demonstrated that it is at the folding-dominated end of fold-and-thrust belt. Therefore, we limit our discussion below to the limitations and applications of each model (i.e., LaMEM and the SPM) to the ZFB.

5.3.1. Limitation of the Mechanical Model and Its Application to the ZFB

Indeed the deformation style of the ZFB has often been explained by buckling of the sedimentary cover above a basal weak layer, represented by the Hormuz salt [e.g., *Colman-Sadd*, 1978; *Mouthereau et al*., 2012; *Yamato et al*., 2011]. The largest detachment folds are observed in the Fars Arc where the salt layer reaches up to 2 km in thickness [*Colman-Sadd*, 1978]. Seismic data [*Jahani et al*., 2009] suggested that there is no relationship between folding and major thrust ramps, and that the cover folding primarily results from the growth of buckle folds (see *Mouthereau et al*. [2012] for a review and discussion about the deformation style in the ZFB; *Schmalholz et al*. [2002]). In the Fars province, the fold pattern is characterized by regular, quasi-periodic folds, with wavelength of 15 km in average [*Mouthereau et al*., 2007; *Yamato et al*., 2011] and axial lengths than can be longer than 100 km [*Mouthereau et al*., 2007]. *Ramsey* [2008] proposed that those long train folds actually result from the lateral propagation and linkage of small segments. These folds characteristics are reproduced in our simulations (Figure 3). However, the thickness ratio between overburden and salt used in our simulations is different that the one observed in the Fars Province. The choice of such a ratio is partly related to the findings discussed in *Yamato et al*. [2011], who used a 2-D numerical model with a visco-elasto-plastic rheology. They used the same thickness ratio as the one of the stratigraphy proposed for the Fars Province, and showed that in order to reproduce the characteristic fold wavelength, growth rate, and morphology of the fold in this area, they should consider weak layers within the overburden and have a rather small friction angle of the brittle materials. As we use linear viscous rheologies, we need to employ a thicker detachment level in order to obtain similar growth rates and wavelengths to the one obtained by *Yamato et al*. [2011] with nonlinear materials.

5.3.2. Limitation of the Surface Processes Model and Its Application to the ZFB

Pounding of syntectonic sediments occurs preferentially behind those long anticlines, and was already observed in previous numerical models [*Tucker and Slingerland*, 1996] or in the field [*James and Wynd*, 1965; *Oberlander*, 1965]. Moreover, transport-limited conditions would generally be favored by more erodible rocks, inefficient transport, and large gravel fraction, as well as at high drainage areas, and reciprocally for detachment-limited conditions [*Whipple and Tucker*, 2002]. Indeed, annual precipitation rates in the Fars Province are low and easily erodible formations (e.g., shales, marls, flysch) are common [*James and Wynd*, 1965; *Oberlander*, 1965]. The Bakhtiari Fm, which is associated with folding and thickening of the ZFB [*Falcon*, 1974; *James and Wynd*, 1965], consists of sandstones and conglomerates, which may contain large pebbles. In addition several geomorphic studies [*Burberry et al*., 2010; *Ramsey et al*., 2008] showed the presence of wind gaps, reflecting the deflection of rivers around the growing anticlines, and thus an inefficient transport. Those geomorphic features can be as well observed in our simulations (e.g., Figure 9, experiments 14 and 15). Finally digital elevation model and ArcGIS analyses also reveal a longitudinal drainage network, as well as high contributive drainage areas for the Mand river, in the Fars. Figure 13 shows a digital elevation model the ZFB, which gives a natural comparison for our simulations.

6. Conclusions

We presented a fully coupled, 3-D numerical model, which was used to study the interactions between surface processes and multilayer folding. The mechanical model considers variations in density and viscosity of an upper crust, and represents a sedimentary cover, with internal weak layers, detached over a much weaker basal layer, representing salt or evaporites. Applied compression results in a series of buckle folds, of which the topographic expression consists of anticlines and synclines. This topography is modified through time by mass redistribution, which is achieved by a combination of fluvial and hillslope erosion, as well as deposition.

The current study has shown that the surface processes have a rather minor effect on folding patterns, which are primarily controlled by the distribution of the random (or prescribed) perturbations and the physics of the folding instability. Their main contribution is due to their ability to strongly modify the initial topography, prior to deformation. However, they have an obvious and strong effect in enhancing folding by gravity, due to filling and loading of synclines and unloading of anticlines, which results in an overall faster growth of the folds. Fluvial incision can, under certain conditions, localize the deformation; leading to the disappearance of some tectonic features such as fold linkage, which would affect in return the sediment routine, as well as the location of the deposition centers.

The model can be applied to the Zagros Folded Belt, which could be comparable to experiments 2, 5, and 8. The quasi-cylindrical character of the Fars long anticlines, in combination with the persistence of small, high aspect ratio doubly plugging structures, would suggest that an initial slope between 0% and 0.1% (experiments 2 and 5) may have been initially present.

Acknowledgments

The high-resolution simulations presented here have been performed on JUQUEEN, on project hmz30. M. Collignon was funded by the European Union FP7 Marie Curie ITN "TOPOMOD," contract 26517. B. Kaus and N. Fernandez were funded by the ERC Starting grant 258830. The authors are thankful to S. Castelltort, G. Simpson, and L. Goren for their comments and discussions on surface processes models, as well as M. Frehner for discussions on folds modeling. Sascha Brune and an anonymous reviewer are thanked for their helpful reviews.

References

Amestoy, P. R., I. S. Duff, and J. Y. L'Excellent (2000), Multifrontal parallel distributed symmetric and unsymmetric solvers, *Comput. Methods Appl. Mech. Eng.*, *184*, 501–520.

Avouac, J. P., and E. B. Burov (1996), Erosion as a driving mechanism of intracontinental mountain growth, *J. Geophys. Res.*, *101*, 17,747–17,769.

Balay, S., J. Brown, K. Buschelman, W. D. Gropp, D. Kaushik, M. G. Knepley, L. Curfman McInnes, B. F. Smith, and H. Zhang (2012), Portable, Extensible Toolkit for Scientific Computation. [Available at http://www.mcs.anl.gov/petsc.]

Barrier, L., T. Nalpas, D. Gapais, J. N. Proust, A. Casas, and S. Bourquin (2002), Influence of syntectonic sedimentation on thrust geometry. Field examples from the Iberian Chain (Spain) and analogue modelling, *Sediment. Geol.*, *146*, 91–104.

Beaumont, C., P. Fullsack, and J. Hamilton (1992), Erosional control of active compressional orogens, in *Thrust Tectonics*, edited by K. R. McClay, pp. 1–18, Chapman and Hall, London, U. K.

Biot, M. A. (1961), Theory of folding of stratified viscoelastic media and its applications in tectonics and orogenesis, *Bull. Geol. Soc. Am.*, *72*, 1595–1620.

Bonnet, C., J. Malavieille, and J. Mosar (2007), Interactions between tectonics, erosion and sedimentation during the recent evolution of the Alpine orogen: Analogue modeling insights, *Tectonics*, *26*, 1–15.

Braun, J. (2006), Recent advances and current problems in modelling surface processes and their interaction with crustal deformation, in *Analogue and Numerical Modelling of Crustal-Scale Processes*, edited by S. J. H. Buiter and G. Schreurs, pp. 307–325, Geol. Soc. of London, London, U. K.

Braun, J., and M. Sambridge (1997), Modelling landscape evolution on geological time scales: A new method based on irregular spatial discretization, *Basin Res.*, *9*, 27–52.

Braun, J., and P. Yamato (2010), Structural evolution of a three-dimensional, finite-width crustal wedge, *Tectonophysics*, *484*, 181–192.

Braun, J., and S. D. Willett (2013), A very efficient O(n), implicit and parallel method to solve the stream power equation governing fluvial incision and landscape evolution, *Geomorphology*, *180–181*, 170–179.

Burbank, D. (2002), Rates of erosion and their implications for exhumation, *Mineral. Mag.*, *66*(1), 25–52.

Burberry, C. M., J. W. Cosgrove, and J. G. Liu (2010), A study of fold characteristics and deformation style using the evolution of the land surface: Zagros Simply Folded Belt, Iran, in *Tectonic and Stratigraphic Evolution of Zagros and Makran During the Mesozoic-Cenozoic*, edited by P. Leturmy and C. Robin, Geol. Soc. of London, London, U. K.

Burg, J. P., B. J. P. Kaus, and Y. Y. Podladchikov (2004), Dome structures in collision orogens: Mechanical investigation of the gravity/compression interplay, in *Gneiss Domes in Orogeny*, edited by D. L. Whitney, C. Teyssier, and C. S. Siddoway, pp. 47–66, Geol. Soc. of Am. Spec. Pap., Boulder, Colo.

Chase, C. G. (1992), Fluvial landsculpting and the fractal dimension of topography, *Geomorphology*, *5*, 39–57.

Cobbold, P. R. (1976), Fold shapes as functions of progressive strain, *Philos. Trans. R. Soc. London A*, *283*, 129–138.

Colman-Sadd, S. P. (1978), Fold development in Zagros Simply Folded Belt, southwest Iran, *AAPG Bull.*, *62*, 984–1003.

Crameri, F., H. Schmeling, G. J. Golabek, T. Duretz, R. Orendt, S. J. H. Buiter, D. A. May, B. Kaus, T. V. Gerya, and P. J. Tackley (2012), A comparison of numerical surface topography calculations in geodynamic modelling: An evaluation of the 'sticky air' method, *Geophys. J. Int.*, *189*, 38–54.

Culling, W. E. H. (1960), Analytical theory of erosion, *J. Geol.*, *68*(3), 336–344.

Davy, P., and D. Lague (2009), Fluvial erosion/transport equation of landscape evolution models revisited, *J. Geophys. Res.*, *114*, F03007, doi:10.1029/2008JF001146.

Eisenstat, S. C., H. C. Elman, and H. C. Schultz (1983), Variational iterative methods for non-symmetric systems of linear equations, *SIAM J. Numer. Anal.*, *20*, 345–357.

Falcon, N. (1974), Southern Iran: Zagros Mountains, in *Mesozoic-Cenozoic Orogenic Belts*, vol. 4, edited by A. Spencer, pp 199-211, *Spec. Publ. Geol. Soc. London*, *4*(1), London, U. K.

Falgout, R., T. Kolev, J. Schroder, P. Vassilevski, and U. Yang (2013), Hypre: High Performance Preconditioners. [Available at http://computation.llnl.gov/casc/linear_solvers/sls_hypre.html.]

Fernandez, N., and B. J. P. Kaus (2014), Fold interaction and wavelength selection in 3D models of multilayer detachment folding, *Tectonophysics*, doi:10.1016/j.tecto.2014.06.013.

Fillon, C., R. S. Huismans, and P. Van der Beek (2013), Syntectonic sedimentaion effects on the growth of fold-and-thrust belts, *Geology*, *41*, 83–86.

Fletcher, R. C. (1991), Three-dimensional folding of an embedded viscous layer in pure shear, *J. Struct. Geol.*, *13*(1), 87–96.

Fletcher, R. C. (1995), Three-dimensional folding and necking of a power-law layer: Are folds cylindrical, and, if so, do we understand why?, *Tectonophysics*, *247*, 65–83.

Garcia-Castellanos, D., J. Vergés, J. M. Gaspar-Escribano, and S. Cloetingh (2003), Interplay between tectonics, climate, and fluvial transport during the Cenozoic evolution of the Ebro Basin (NE Iberia), *J. Geophys. Res.*, *108*(B7), 2347, doi:10.1029/2002JB002073.

Goren, L., S. D. Willett, F. Herman, and J. Braun (2014), Coupled numerical-analytical approach to landscape evolution modeling, *Earth Surf. Processes Landforms*, *39*, 522–545.

Graveleau, F. (2008), *Interactions Tectoniques, Erosion, Sédimentation Dans les Avant-Pays de Chaines: Modélisation Analogique et étude des Piémonts de l'est du Tian Shan (Asie Centrale)*, 487 pp., Univ. de Montpellier II, Montpellier, France.

Howard, A. D., and G. Kerby (1983), Channel changes in badlands, *Geol. Soc. Am. Bull.*, *94*, 739–752.

Jahani, S., J.-P. Callot, J. Letouzey, and D. Frizon de Lamotte (2009), The eastern termination of the Zagros Fold-and-Thrust Belt, Iran: Structures, evolution, and relationships between salt plugs, folding, and faulting, *Tectonics*, *28*, TC6004, doi:10.1029/2008TC002418.

James, G. A., and J. G. Wynd (1965), Stratigraphic nomenclature of Iranian oil consortium agreement area, *Am. Assoc. Pet. Geol. Bull.*, *49*, 2162–2245.

Kaus, B. J. P., and S. M. Schmalholz (2006), 3D finite amplitude folding: Implications for stress evolution during crustal and lithospheric deformation, *Geophys. Res. Lett.*, *33*, L14309, doi:10.1029/2006GL026341.

Kaus, B. J. P., C. Steedman, and T. W. Becker (2008), From passive continental margin to mountain belt: Insights from analytical and numerical models and applicaiton to Taiwan, *Phys. Earth Planet. Inter.*, *171*, 235–251.

Kaus, B. J. P., A. Popov, and D. A. May (2012), Recent progress in modelling 3D lithospheric deformation, paper presented at EGU Spring Meeting, Vienna. [Available at http://meetingorganizer.copernicus.org/EGU2012/EGU2012-14116.pdf.]

Konstantinovskaia, E., and J. Malavieille (2005), Erosion and exhumation in accretionary orogens: Experimental and geological approaches, *Geochem. Geophys. Geosyst.*, *6*, Q02006, doi:10.1029/2004GC000794.

Kooi, H., and C. Beaumont (1994), Escarpment evolution on high-elevation rifted margins: Insights derived from a surface processes model that combines diffusion, advection, and reaction, *J. Geophys. Res.*, *99*, 12,191–12,209.

Lechmann, S. M., D. A. May, B. J. P. Kaus, and S. M. Schmalholz (2011), Comparing thin-sheet models with 3-D multilayer models for continental collision, *Geophys. J. Int.*, *187*, 10–33.

Malavieille, J. (2010), Impact of eosion, sedimentation, and structural heritage on the structure and kinematics of orogenic wedges: Analog models and case studies, *GSA Today*, *20*(1), 4–10.

Mancktelow, N. S. (2001), Single-layer folds developed from initial random perturbations: The effects of probability distribution, fractal dimension, phase and amplitude, in *Tectonic Modeling: A Volume in Honor of Hans Ramberg*, edited by H. A. Koyi and N. S. Mancktelow, pp. 69–87, Geol. Soc. of Am. Mem., Boulder, Colo.

Molnar, P., and P. England (1990), Late Cenozoic uplift of mountain ranges and global climate change: Chicken or egg?, *Nature*, *346*, 29–34.

Montgomery, D. R., and M. T. Brandon (2002), Topographic controls on erosion rates in tectonically active mountain ranges, *Earth Planet. Sci. Lett.*, *201*, 481–489.

Mouthereau, F., O. Lacombe, J. Tensi, N. Bellahsen, S. Kargar, and K. Amrouch (2007), *Mechanical constraints on the development of the Zagros Folded Belt (Fars), in* Thrust Belts and Foreland Basins: From Kinematics to Hydrocarbon Systems: Frontiers in Earth Sciences, edited by O. Lacombe, J. Roure, and J. Vergés, pp. 245–264, Springer, Berlin.

Mouthereau, F., O. Lacombe, and J. Vergés (2012), Building the Zagros collisional orogens: Timing, strain distribution and dynamics of Arabia/Eurasia plate convergence, *Tectonophysics*, *532–535*, 27–60.

Mugnier, J.-L., P. Baby, B. Colleta, P. Vinour, P. Bale, and P. Leturmy (1997), Thrust geometry controlled by erosion and sedimentation: A view from analogue models, *Geology*, *25*, 427–430.

Mukherjee, S., C. J. Talbot, and H. A. Koyi (2010), Viscosity estimates of salt in the Hormuz and Namakdan salt diapirs, Persian Gulf, *Geol. Mag.*, *147*(04), 497–507.

Nalpas, T., I. Györfi, F. Guillocheau, F. Lafont, and P. Homewood (1999), Influence of sediment loading on growth folds. Analogue modelling and field study (southern border of the Jaca basin), *Bull. Soc. Geol. Fr.*, *170*(5), 733–740.

Nalpas, T., D. Gapais, J. Vergés, L. Barrier, V. Gestain, G. Leroux, D. Rouby, and J. J. Kermarrec (2003), Effects of rate and nature of synkinematic sedimentation on the growth of compressive structures constrained by analogue models and field examples, *Geol. Soc. Spec. Publ.*, *208*, 307–319.

Oberlander, T. M. (1965), *The Zagros Streams: A New Interpretation of Transverse Drainage in an Orogenic Zone*, Syracuse Univ. Press, New York.

Oberlander, T. M. (1985), Origin of drainage transverse to structures in orogens, in *Tectonic Geomorphology, Binghamton Symposia in Geomorphology*, vol. 15, pp. 155, Unwin Hyman, Boston.

O'Callaghan, J. F., and D. M. Mark (1984), The extraction of drainage networks from digital elevation data, *Comput. Vision Graphics Image Process.*, *28*, 323–344.

Perron, J. T., J. W. Kirchner, and W. E. Dietrich (2008), Spectral signatures of characteristic spatial scales and nonfractal structure in landscapes, *J. Geophys. Res.*, *113*, F04003, doi:10.1029/2007JF000866.

Persson, K. S., and D. Sokoutis (2002), Analogue models of orogenic wedges controlled by erosion, *Tectonophysics*, *356*(4), 323–336.

Pichot, T., and T. Nalpas (2009), Influence of synkinematic sedimentation in a thrust system with two decollement levels; analogue modelling, *Tectonophysics*, *473*, 466–475.

Popov, A., and B. Kaus (2013), LaMEM (Lithosphere and Mantle Evolution Model): Advancing a staggered-grid finite difference version of the code, paper presented at EGU, Vienna. [Available at http://meetingorganizer.copernicus.org/EGU2013/EGU2013-7761.pdf.]

Ramberg, H. (1964), Selective buckling of composite layers with contrasted rheological properties, *Tectonophysics*, *1*, 307–341.

Ramsey, L. A., R. T. Walker, and J. Jackson (2008), Fold evolution and drainage development in the Zagros mountains of Far provinces, SE Iran, *Basin Res.*, *20*, 23–48.

Ruh, J. B., B. J. P. Kaus, and J. P. Burg (2012), Numerical investigation of deformation mechanics in fold-and-thrust belts: Influence of rheology of single and multiple décollements, *Tectonics*, *31*, 1–23.

Ruh, J. B., T. V. Gerya, and J. P. Burg (2013), High-resolution 3D numerical modeling of thrust wedges: Influence of décollement strength on transfer zones, *Geochem. Geophys. Geosyst.*, *14*, 1131–1155, doi:10.1002/ggge.20085.

Saad, Y. (2003), *Iterative Methods for Sparse Linear Systems*, SIAM, Philadelphia, Pa.

Schmalholz, S. M., and Y. Podladchikov (2000), Finite amplitude folding: Transition from exponential to layer length controlled growth, *Earth Planet. Sci. Lett.*, *179*, 363–377.

Schmalholz, S. M., Y. Podladchikov, and J. P. Burg (2002), Control of folding by gravity and matrix thickness: Implications for alrge-scale folding, *J. Geophys. Res.*, *107*(B1), doi:10.1029/2001JB000355.

Schmid, D. W., and Y. Podladchikov (2006), Fold amplification rates and dominant wavelength selection in multilayer stacks, *Philos. Mag. A*, *86*(21–22), 3409–3423.

Schmid, D. W., M. Dabrowski, and M. Krotkiewski (2008), Evolution of large amplitude 3D fold patterns: A FEM study, *Phys. Earth Planet. Inter.*, *171*, 400–408.

Simpson, G. (2004a), A dynamic model to investigate coupling between erosion, deposition, and three-dimensional (thin-plate) deformation, *J. Geophys. Res.*, *109*, F02006, doi:10.1029/2003JF000078.

Simpson, G. (2004b), Role of river incision in enhancing deformation, *Geology*, *32*, 341–344.

Simpson, G. (2004c), Dynamic interactions between erosion, deposition, and three-dimensional deformation in compressional fold belt setting, *J. Geophys. Res.*, *109*, F03007, doi:10.1029/2003JF000111.

Simpson, G. (2006), Modelling interactions between fold-thrust belt deformation, foreland flexure and surface mass transport, *Basin Res.*, *18*, 125–143.

Simpson, G., and F. Schlunegger (2003), Topographic evolution and morphology of surfaces evolving in repsonse to coupled fluvial and hillslope sediment transport, *J. Geophys. Res.*, *108*(B6), 2300, doi:10.1029/2002JB002162.

Smith, T. R., and F. P. Bretherton (1972), Stability and the conservation of mass in drainage basin evolution, *Water Resour. Res.*, *8*, 1506–1529.

Storti, F., and K. McClay (1995), Influence of syntectonic sedimentation on thrust wedges in analog models, *Geology*, *23*, 999–1002.

Thieulot, C., and R. S. Huismans (2011), FANTOM3Dsp: Coupling a thermo-mechanically coupled 3D creeping flow solver with a surface processes model, paper presented at EGU Spring Meeting, Vienna. [Available at http://meetingorganizer.copernicus.org/EGU2011/EGU2011-10833.pdf.]

Tucker, G. E., and R. Slingerland (1996), Predicting sediment flux from fold and thrust belts, *Basin Res. 8*, 329–349.

Tucker, G. E., and K. X. Whipple (2002), Topographic outcomes predicted by stream erosion models: Sensitivity analysis and intermodel comparison, *J. Geophys. Res.*, *107*(B9), 2179, doi:10.1029/2001JB000162.

Whipple, K. X., and G. E. Tucker (1999), Dynamics of the stream-power river incision model: Implications for height limits of mountain range, landscape response timescales, and research needs, *J. Geophys. Res.*, *104*, 17,661–17,674.

Whipple, K. X., and G. E. Tucker (2002), Implications of sediment-flux-dependent river incision models for landscape evolution, *J. Geophys. Res.*, *107*(B2), doi:10.1029/2000JB000044.

Willett, S. D. (1999), Orogeny and orography: The effects of erosion on the structure of mountain belts, *J. Geophys. Res.*, *104*, 28,957–28,981.

Willett, S. D. (2010), Erosion on a line, *Tectonophysics*, *484*, 168–180.

Yamato, P., B. Kaus, F. Mouthereau, and S. Castelltort (2011), Dynamic constraints on the crustal-scale rheology of the Zagros fold belt, Iran, *Geology*, *39*, 814–818.

Zienkiewicz, O. C., and R. L. Taylor (2000), *The Finite Element Method,* vol. 1*,* The Basis, Butterworth-Heinemann, Woburn, Mass.